



New insights on the expediency of Egyptian organoclays to suppress corrosiveness of acidic-produced water in Abu-Rudeis oilfield, South Sinai, by removal of scale-forming cations and sulfate-reducing bacteria: Is there a direct link to clay lamellar ordering?

Amr A. Hassan, Ashraf A. Mohamed, (The Late) Abdel-Moneim Barakat[†], Atef S. Darwish*

Department of Chemistry, Faculty of Science, Ain Shams University, 11566 Cairo, Egypt, Tel. +20 22-483-1836;
email: atef_mouharam@sci.asu.edu.eg (A.S. Darwish)

Received 17 April 2020; Accepted 28 July 2020

ABSTRACT

This study focused on resolving the query “which is the most beneficial clay system for the petroleum industry, intercalated or exfoliated”? Dimethyl sulfoxide (DMSO) and ethylenediaminetetraacetate ions (EDTA²⁻) were used as well-known agents in the tailoring of intercalated- and exfoliated-organoclays, respectively. Both systems were characterized by X-ray diffraction, Fourier-transform infrared spectroscopy, dynamic light scattering, N₂-physisorption, transmission electron microscopy, and atomic force microscopy techniques, and examined in treating oilfield produced water. EDTA-clay exhibited long-term ordered, uniformly negatively charged, and high swellable tactoids of hexagon shapes with enhanced pore structure. The lamellar structure of DMSO-clay was highly degenerated and roughened conducting uneven highly charged particles of poor surface features. EDTA-clay was preferentially managed in the petroleum industry as a perfectly safe and efficient agent for (i) long-lasting removal of scale-forming cations (Fe³⁺, Mg²⁺, Ca²⁺, and Sr²⁺) from oilfield produced water with high adsorption rates yielding performances ≥85% within excellent six repeating regeneration/reuse runs, (ii) corrosion protection of steel pipelines, and (iii) killing of sulfate-reducing bacteria (near 100%). Increased demand for exploration of multidiscipline materials for the petroleum industry will revitalize clay intercalation systems to a magnificent renaissance.

Keywords: Intercalated clay system; Oilfield produced water; Sulfate-reducing bacteria; Steel corrosion

1. Introduction

Oilfield produced water is massively drawn from the ground during petroleum production and exploration, whereas the amount of water may be tenfold the quantity of oil produced [1]. Most of the produced water has an acidic character with very high salt concentration and contains numerous organic and inorganic pollutants [2]. Unfortunately, such unwanted water is inevitably discharged into the environment during oil exploitation, extraction, and processing thus causes extensive environmental

contamination, which can seriously destroy the ecological balance and affect human health [1,3]. By increasing the global demand for a clean environment and the stringent environmental regulations to date [4], most of the researchers' approaches for the management of produced water focus on sequential injection of water into oil-reservoir for pressure maintenance adopting a mechanism designated as “secondary oil recovery” [2,5,6]. A processing system that is frequently used in Sinai oil fields, Fig. 1. Inspection of literature, the several previous attempts for recycling and usage of produced water in various applications like crop

* Corresponding author.

[†] Passed away on April 2017.

This paper is dedicated to the memory of Dr. Abdel-Moneim Barakat for his kind inspiration of this work.

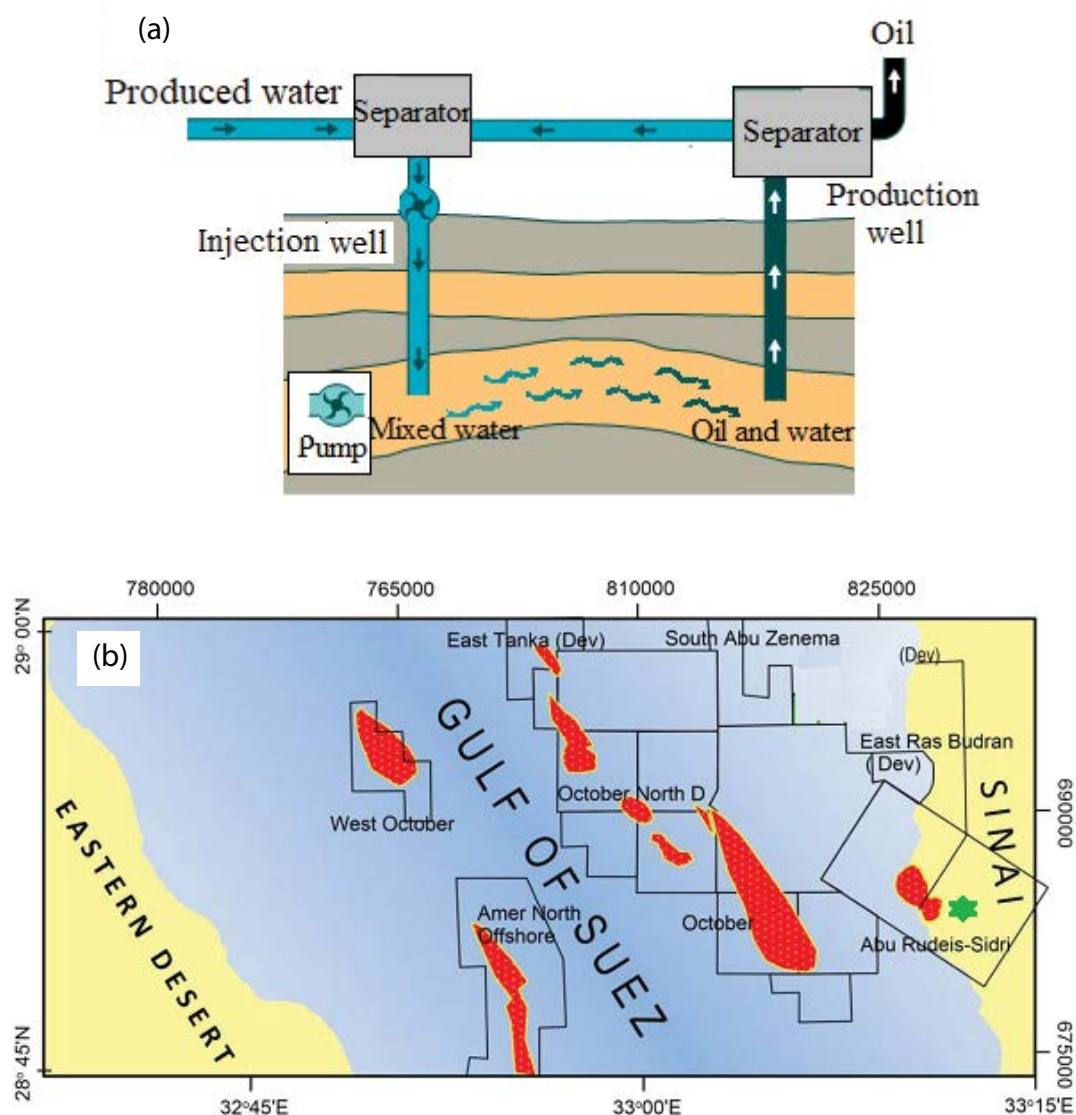


Fig. 1. (a) Water injection route of oil production in shale and (b) location map of the major oilfield stations in South Sinai, Egypt. The green-six horns represent the Abu-Rudeis oilfield.

irrigation, wildlife and livestock consumption, aquaculture and hydroponic vegetable culture, dust control, vehicle, and equipment washing, power generation, and fire control, seem to face great failure because of the presence of tolerable contents of organic and/or inorganic pollutants in the recycled oilfield produced water, restricting, thereby, from discharging of treated produced water into the environment [1,2,7,8]. Despite the pleasurable availability with which produced water spreads through an oil-bearing formation and waters' efficiency in displacing oil [5], the resulted injecting water becomes the key point for corrosion of pipelines system used in the petroleum industry [9–11], and the formation of oilfield mineral scale deposits [12,13].

The corrosion behavior of steel pipelines is a significant complicated flow assurance problem in petroleum industry due to dissolution of metallic iron adopting several scenarios: (i) the continual injection of produced water into oil wells elevates the levels of sulfate and chloride ions in the

produced water converting it to corrosive "acidified" water that capable to interact with the internal walls of pipelines forming iron ions in the production fluids during tubing operation [9,13–15], (ii) the presence of various operations, for example, production, water injection and workover operations, in oil industry realizes the requirements needed for corrosion cell in oilfield pipelines, as dissolution of iron ($\text{Fe}(s) \rightleftharpoons \text{Fe}^{3+}(\text{aq})$) occurs at anodic sites with sequential supplying by various electron acceptors such as chlorine, oxygen and hydrogen ions in aqueous fluid for cathodic process [10,16], and (iii) the abundant occurrence of anaerobic sulfate-reducing bacteria (SRB) in oilfield produced water positively influences corrosion of steel pipelines, by reducing sulfate to sulfide, and oxidizing metallic iron to ferrous ions [11,17]. In addition, the ferrous ions produced by various corrosion reactions may strongly deposit as scale on the corroding metal surface, leading probably to blockage of tubing or pipelines [10,16].

On the other hand, one of the common problematic issues in the oil industry is the formation of mineral scales such as calcium carbonate, calcium sulfate, and magnesium carbonate [17]. Mineral scales are hard crystalline inorganic salts formed by a process of deposition from the produced water supersaturated with minerals as a result of the changes in the operating conditions, that is, ionic composition, pH, pressure, and temperature [12–15]. Salt deposition can occur during the fluid flow in the reservoir, wellbore as well as wellhead in petroleum operations causing significant deterioration of various oil development processes, that is, reduction of production rate and well productivity, plugging the perforations, and premature failure of downhole equipment [15,17].

Under the slogan of “prevention is better than cure”, considerable works have been carried out to reduce the levels of scale-forming cations (Fe^{3+} , Mg^{2+} , and Ca^{2+} ions) in the oilfield produced water through conducting ultra-filtration membranes [18,19], electrocoagulation/flotation and electrodialysis cells [20–23], and designing of efficient adsorbents, viz. activated carbon, ion-exchange resin, functionalized polymers and organoclays [24,25]. Furthermore, previous researches were conducted on decreasing the activity of SRB by treatment of produced water with various biocides [26]. Unfortunately, most of the synthesized membranes can be seriously polluted during the purification operation associated with a poor possibility of regeneration [20], and the electrocoagulation technique is still under development. Meanwhile, most of the used adsorbents in literature have just functioned to selective removal of certain mineral ions from oilfield produced water linked with insignificant adsorption efficiency and poor biocide activity toward SRB [25,27]. As presented by all previous reports conducted so far, no sounding choices have been yet landmarked in the field of treatment of produced water in the oil industry, opening the door toward more sincere efforts by scientists throughout the world.

In the past few years, the treatment of wastewaters by various organically modified clay systems has gained much attention due to the ease-reforming of clay lamellar structure generating either intercalated or exfoliated or intercalated/exfoliated systems, and the capability of inter-lamellar spaces to contain organic molecules [28–31]. These given advantageous to clay sheets potentially enhance their efficiency and durability toward the removal of generic unwanted cations and/or anions from wastewater, and their biocide activity [32–34]. Among the whole reported organo-modifiers in literature, those who possess amphiphilic or anionic character have drawn mounting attention from researchers [35,36]. By considering dimethyl sulfoxide (DMSO) as a common polar aprotic modifier with good tendencies to accept hydrogen bond, it is widely employed for the expansion of clay interlayered spaces giving way to developing physico- and mechano- chemical properties of clay for efficient usages in several industrial and environmental fields [36–39]. On the other hand, the presence of ethylenediaminetetraacetate anion (EDTA^{2-}) in clay sheets are judiciously chosen as an efficient intercalant molecule, which increases from the scavenging action of clay to various hazard cations in wastewater [35,40,41].

To the best of our knowledge, this study, for the first time in literature, aims to recognize the capability of DMSO- and EDTA-organoclays to remove the most common scale-forming cations, particularly Fe^{3+} , Mg^{2+} , Ca^{2+} , and Sr^{2+} ions, and the SRB species from the oilfield produced water with ruling out the role of clay lamellar architecture in upgrading their performances. Besides, the most efficient clay lamellar model in scaling ions' removal is examined as an anticorrosion agent for steel pipelines.

2. Experimental setup

2.1. Materials

High-grade natural bentonite was supplied by the Pico Petroleum Service Company (PICO) from Sinai, Egypt. The representative sample was crushed, ground, sieved to 200 mesh size, and dried at 110°C . Its chemical composition as determined by X-ray fluorescence in wt.% is MgO , 0.03; CaO , 0.30; SiO_2 , 44.31; Fe_2O_3 , 2.31; K_2O , 0.08; Na_2O , 0.03; Al_2O_3 , 36.97; TiO_2 , 1.33; loss on ignition, 14.67. This clay mainly comprises of low-defect bentonite (98 wt.%) with a Hinckley index of around 0.4. Its cation exchange capacity and specific surface area are 19 meq/100 g and $37\text{ m}^2/\text{g}$, respectively, as determined using standard methods [42,43].

The edetate disodium (EDTA^{2-}), DMSO, ferric chloride ($\text{FeCl}_3 \cdot 6\text{H}_2\text{O}$), magnesium chloride ($\text{MgCl}_2 \cdot 6\text{H}_2\text{O}$), calcium chloride ($\text{CaCl}_2 \cdot 2\text{H}_2\text{O}$), and strontium chloride ($\text{SrCl}_2 \cdot 6\text{H}_2\text{O}$) were purchased from Sigma-Aldrich Co., (St. Luis, MO, USA). Other used chemicals in this study were of analytical grade. Deionized water was used for the preparation of solutions, wherever required.

2.2. Synthesis and characterization of organo-modified clay samples

The natural bentonite clay (25 g) was purified by being overnight refluxed with 500 mL of 1 M nitric acid solution, adopting a bentonite/acid mass ratio close to 1:1 to limit clay delamination [31]. The resulting activated clay was centrifuged and washed with deionized water several times and dried at 150°C . The acid-treated (purified) bentonite clay was taken as a reference clay sample and coded as “R-B”.

For the synthesis of bentonite clay modified by edetate disodium salt, 10 g of R-B were soaked in 500 mL of EDTA^{2-} solution (0.024 M) under vigorous stirring at 60°C overnight. To encourage swelling and dispersion of clay layers, the pH of this mixture was adjusted at 5.0, and the clay concentration was kept at $<2\%$ (wt./wt.). The mixture was then filtered and complete removal of EDTA from the supernatant was confirmed by using the complexometric titration method described elsewhere [41]. Afterwards, the produced organo-modified clay (EDTA-B) was washed several times with deionized water and dried at 110°C for 24 h. Finally, the obtained solid fractions (EDTA: clay = 8 wt.%) were crushed, ground, and screened to a particle size $<2\ \mu\text{m}$.

For preparing of bentonite clay modified by DMSO molecules (DMSO-B), 10 g of R-B were soaked in 500 mL of DMSO solution (0.051 M) under vigorous stirring at 60°C for 18 h, keeping the clay concentration at $<2\%$ (wt./wt.) linked

with DMSO to clay mass ratio of 1:2.5. The remaining experimental steps complied with those above-mentioned in the preparation of the EDTA-B clay sample. Complete removal of DMSO molecules from the supernatant was conceived by the disappearance of its characteristic sulfoxide peak at $1,044\text{ cm}^{-1}$ using Fourier-transform infrared spectroscopy (FTIR) spectrometry method [44].

The structural features of reference clay (R-B) and organoclays (EDTA-B and DMSO-B) was performed using (i) X-ray diffraction (XRD) Phillips PW3710-BASED diffractometer (The Netherlands) operating at 40 kV and 55 mA using Ni-filtered $\text{CuK}\alpha$ radiation ($\lambda = 1.5418\text{ \AA}$), and (ii) FTIR Mattson ATI Genesis Spectrometer (USA), with a nominal resolution of 2 cm^{-1} . The surface potentials of the as-prepared clay samples were measured using the Zetasizer Nano Series (MALVERN, United Kingdom), as being described in previous work [28]. The zeta potential values (ζ) were evaluated at 25°C , as a function of pHs from 3.0 to 8.0. The hydrodynamic diameters were investigated by dynamic light scattering (DLS) using the previously described Zetasizer Nano Series Instrument [28]. Zeta-potential distribution curves as well as average particle size were also detected at 25°C with adjusting pH at 3.0 (industrial employment conditions during oilfield produced water treatment). The textural characteristics of clay samples under study were investigated by the aid of N_2 adsorption–desorption isotherms measured at -196°C , for surface area determination and pore size analysis [43,45]. A NOVA 3200 apparatus (USA) was used, where the samples were outgassed at 150°C for 4 h at 10^{-5} Torr [43,45]. The morphological features were recognized adopting (i) high-resolution transmission electron microscopy (HR-TEM, JEOL-2100, Japan), operating at 200 kV with a resolution of 0.14 nm, and (ii) atomic force microscopy (AFM, Agilent 5500, USA) with a sharpened silicon nitride SI-DF20 cantilever of a force constant of 0.12 Nm^{-1} and a resonance frequency of about 3 kHz. The produced AFM topographic image ($5\text{ }\mu\text{m} \times 5\text{ }\mu\text{m}$ scan size) was analyzed for the quantitative estimation of the height in the z-dimension (Z), as well the surface roughness, using the inbuilt image analysis software supplied by the AFM [32].

The swelling index (SI) test was chosen to assess the swelling character of the as-prepared organoclays. To perform this test, 2 g of each understudied organoclay was finely ground and sieved to 100 mesh-size. The SI test is performed by sprinkling the clay on the water surface in a 100 mL filled graduated cylinder, as per the SI test requirements. The SI is the settled volume of clay after 24 h of settling [23].

2.3. Produced water sampling and characterization

Oilfield produced water (OPW) samples were collected from the upstream pipelines in Abu-Rudeis oilfield (South Sinai, Egypt) in February 2019. The area under investigation is located between latitudes $28^\circ56'\text{N}$ – $28^\circ84'\text{N}$ and longitudes $33^\circ06'\text{E}$ – $33^\circ14'\text{E}$ (Fig. 1b). The produced water samples were analyzed for pH, scale-forming cations (Fe^{3+} , Mg^{2+} , Ca^{2+} , and Sr^{2+}), anions (Cl^- and SO_4^{2-}) and total dissolved solids (TDS) using standard methods described elsewhere [24]. The properties of the tested produced water samples were listed in Table 1. The interval values of acidity as well as the concentration of scaling cations were estimated based

on the acquirement of the deterministic lower bound and upper bound in produced water in the oilfield platform.

2.4. Adsorption studies for removal of Fe^{3+} from artificially produced water by under-investigated clays: isotherm, kinetics, and thermodynamic analysis

Batch adsorption was carried out in stoppered 100 mL Erlenmeyer flask. A stock solution of $\text{FeCl}_3 \cdot 6\text{H}_2\text{O}$ (300 mg/L) was prepared in deionized. To provide an artificially produced water, solid salts of sodium chloride and sodium sulfate ($\text{NaCl}:\text{Na}_2\text{SO}_4 = 15\text{ wt.}\%$) with a concentration of 60 g/L were dissolved in the iron(III) stock solution to simulate the real concentration of TDS in Abu-Rudeis oilfield produced water, Table 1. The stock solution was diluted to appropriate concentrations, which were coherent with the recorded interval of Fe^{3+} composition in the oilfield produced water, cf. Table 1.

The standard batch adsorption procedure was followed using a rotary shaker at 150 rpm equipped with a thermostat. In each flask, a constant volume (50 mL) of the appropriate concentration of Fe^{3+} solution was stirred with a constant clay dosage of 2 g/L (solid:liquid) at the chosen temperature and pH values. Each time after completion of the experiment, the solutions were filtered and the equilibrium concentration of Fe^{3+} was analyzed by Agilent 7900 inductively coupled plasma–mass spectrometry system (ICP-MS, Agilent, Santa Clara, CA). In all of the examined experiments, pH, adsorption equilibrium isotherm (initial Fe^{3+} solution concentration), contact time, and temperature were selected as experimental parameters. Adsorption experiments were performed in triplicate, and average values were reported.

2.4.1. Effect of solution pH

The uptake of $\text{Fe}(\text{III})$ by the investigated organoclays was studied at different initial solution pHs ranged from 1.8 to 3.4, meeting the operational conditions in Abu-Rudeis oilfield platform, cf. Table 1, at 298 K for 4 h. The initial Fe^{3+} concentration was managed to be kept at 50 mg/L, being close to the averaged value of the recorded Fe^{3+} concentration interval in oilfield produced water, with a clay dosage of 0.1 g/50 mL. The remained experimental conditions were set up adopting the above-described operation in section 2.4. The removal performance (R , %) of Fe^{3+} ions from artificially produced water by the under-investigated clay samples was calculated (Eq. (1)) as follows:

$$\text{Removal performance}(\%) = \left(\frac{C_0 - C_e}{C_0} \right) \times 100 \quad (1)$$

where C_0 and C_e (mg L^{-1}) were the initial and the equilibrium concentrations of iron(III) solutions, respectively.

2.4.2. Adsorption equilibrium studies and isotherms

The initial $\text{Fe}(\text{III})$ concentrations were kept at 10, 20, 40, 50, 70, 90 and 120 mg/L, that is, the selected values were matched with the operating $\text{Fe}(\text{III})$ concentration range in

Table 1 Sampling number

Analysis for the concentration of scale-forming ions in acidic produced water derived from Abu-Rudeis oilfield, South Sinai, Egypt

Parameter, dimension	Sampling number					Interval values for scale-forming cations and pH	Average values
	1	2	3	4	5		
Ferric ion, mg/L	20	51	23	120	25	20–120	48
Magnesium ion, mg/L	1,054	2,085	1,810	1,540	1,330	1,000–2,100	1,564
Calcium ion, mg/L	1,250	4,458	1,200	4,910	1,750	1,000–5,000	2,713
Strontium ion, mg/L	90	158	24	221	28	20–220	104
pH	3.3	2.7	3.4	1.9	3.1	1.9–3.4	2.8
Chloride ion, mg/L	26,661	38,282	28,360	61,405	24,817		36,500
Sulfate ion, mg/L	2,130	2,750	1,920	3,070	2,400		2,454
Total dissolved solids, g/L	47.50	63.86	49.29	94.53	46.08		60.25

Abu-Rudeis oilfield produced water (Table 1). Batch experiments for sorption of Fe^{3+} from artificially produced water over R-B, DMSO-B and EDTA-B clays were operated at their correspondingly found optimum pHs using clay dosage of 0.1 g/50 mL (solid:liquid) at 298 K for 4 h. The equilibrium concentrations of Fe(III) were measured, following the procedure mentioned in section 2.4., to determine the equilibrium adsorption capacity (q_e , mg g^{-1}) and evaluate adsorption isotherms. The adsorption capacity was calculated by the following formula (Eq. (2)).

$$q_e = (C_0 - C_e) \times \frac{V}{m} \quad (2)$$

where V was the volume of solution (L) and m was the mass of adsorbent (g).

The Freundlich isotherm was valid multilayer sorption on heterogeneous surfaces of an indefinite number of binding sites [46]. The linear form of Freundlich equation (Eq. (3)) may be written as:

$$\ln q_e = \ln(K_F) + \left(\left(\frac{1}{n} \right) \ln C_e \right) \quad (3)$$

where q_e , K_F and n were the equilibrium sorption capacity of Fe^{3+} per unit weight of adsorbent ($\text{mg}^{1-1/n} \text{L}^{1/n} \text{g}^{-1}$), the Freundlich coefficient indicative of the relative adsorption capacity of the adsorbent and the constant correlated to the intensity of adsorption, respectively.

Conversely, Langmuir isotherm was a good-interpreted model for monolayer sorption onto nearly homogeneous surface owing to a finite number of binding sites. It assumed uniform energies of sorption on the surface with marginal interaction between adsorbate molecules [47]. The linear form of Langmuir equation (Eq. (4)) may be expressed as follows:

$$\frac{C_e}{q_e} = \left(\frac{1}{(K_L \times q_m)} \right) + \left(\left(\frac{1}{q_m} \right) \times C_e \right) \quad (4)$$

where q_m and K_L were the monolayer adsorption capacity (mg g^{-1}) and the Langmuir equilibrium coefficient related to

the energy of adsorption (L mg^{-1}), respectively. The essential feature of the Langmuir isotherm model could be explained in terms of a dimensionless constant separation factor (R_L), which was defined by Eq. (5).

$$R_L = \frac{1}{(1 + (K_L \cdot C_0))} \quad (5)$$

The Dubinin–Radushkevich (D–R) equilibrium isotherm model was also used for adsorption data fitting to estimate the apparent free energy (E , kJ mol^{-1}) and the theoretical adsorption saturation capacity (q_D , mg g^{-1}) [48]. The D–R isotherm could be linearized as represented in the following equation:

$$\ln q_e = \ln q_D - \left\{ \left(RT \ln \left(1 + \left(\frac{1}{C_e} \right) \right) \right)^2 / (2E^2) \right\} \quad (6)$$

where R and T were the general gas constant and the adsorption temperature, respectively.

The Temkin isotherm model was also employed as it considered the effect of indirect adsorbate/adsorbate binding interactions in the multi-layered adsorption process [49]. The linear form of the Temkin isotherm model was expressed by Eq. (7) as follows:

$$q_e = (B \cdot \ln K_T) + (B \cdot \ln C_e) \quad (7)$$

where B was a constant related to the heat of adsorption and it was defined by the expression $B = RT/b$, b was the Temkin constant (J mol^{-1}). K_T was the Temkin equilibrium binding coefficient (L g^{-1}).

2.4.3. Effect of contact time (kinetic studies)

In the kinetic experiments, the uptake studies of Fe^{3+} by various under-investigated clay samples were set up at an initial Fe^{3+} concentration of 50 mg/L (matching the averaged Fe^{3+} value in OPW) with a clay dosage of 0.1 g/50 mL at 298 K. The selectively operated solution pHs for the kinetic

studies of R-B, EDTA-B and DMSO-B were subjected at their correspondingly found optimum pHs above-described in section 2.4.1. Aliquots from solutions were taken at different time intervals (8–240 min), and then filtered and analyzed using ICP-MS as being declared previously in section 2.4. The kinetics of the adsorption processes were studied using both pseudo-first-order [49,50] and pseudo-second-order models [51] for the rate expression given, respectively, by:

$$\ln(q_e - q_t) = \ln(q_e) - (k_1 \cdot t) \quad (8)$$

$$\frac{t}{q_t} = \left(\frac{1}{k_2 \cdot q_e^2} \right) + \left(\frac{t}{q_e} \right) \quad (9)$$

where q_t was the adsorption capacity of Fe^{3+} per unit weight of clay at any time t (mg g^{-1}); k_1 represented the pseudo-first-order rate constant (h^{-1}); k_2 was the pseudo-second-order rate constant ($\text{g mg}^{-1} \text{h}^{-1}$).

The possibility of iron(III) diffusion either from liquid bulk phase up to the clay surface or within the pore structure of clay could be described by the Fickian particle diffusion concept using Eq. (10) [50] as given below:

$$q_t = (k_i t^{0.5}) + X \quad (10)$$

where k_i represented the intraparticle diffusion rate constant ($\text{mg g}^{-1} \text{min}^{-0.5}$) and X was constantly related to the presence-absence of the boundary layer effect on the rate of adsorption, which was mutually controlled by film diffusion and intraparticle diffusion.

The Elovich model was worthy applied for recognition of possible Fe^{3+} chemisorption over the energetical adsorption sites of clays under study [51], as being denoted in the following equation:

$$q_t = \beta \ln(\alpha\beta) + (\beta \ln t) \quad (11)$$

where α and β , the Elovich coefficients, represented the initial adsorption rate ($\text{g mg}^{-1} \text{min}^{-2}$) and the desorption coefficient ($\text{g mg}^{-1} \text{min}^{-2}$), respectively.

2.4.4. Effect of temperature (thermodynamic studies)

The thermodynamic parameters of adsorption reaction were obtained by recording q_e and C_e values of the adsorption equilibrium isotherms operated at temperatures 298, 303 and 313 K. The molar enthalpy change (ΔH° , kJ mol^{-1}) and the molar entropy change (ΔS° , kJ mol^{-1}) were calculated using Eq. (12) [51] as given below:

$$\ln\left(\frac{q_e}{C_e}\right) = \left(\frac{\Delta S^\circ}{R}\right) - \left(\frac{\Delta H^\circ}{RT}\right) \quad (12)$$

where q_e/C_e was nominated by the thermodynamic equilibrium constant. Also, Gibbs molar free energy change (ΔG° , kJ mol^{-1}) was calculated using Eq. (13) [51] as mentioned below:

$$\Delta G^\circ = \Delta H^\circ - (T\Delta S^\circ) \quad (13)$$

2.5. Performance and kinetic studies on removal of Mg^{2+} , Ca^{2+} and Sr^{2+} scaling ions from artificially produced water by clay under investigation

Meeting the procedure used in section 2.4. for managing an artificially produced water, aqueous solutions of Mg^{2+} , Ca^{2+} , and Sr^{2+} ions were prepared at concentrations of 1,564; 2,713; and 104 mg/L , respectively. These concentrations were chosen to match their corresponding average values recorded in Abu-Rudeis oilfield produced water (Table 1). The performances (%) of DMSO-B and EDTA-B organo-clays toward the removal of Mg^{2+} , Ca^{2+} , and Sr^{2+} ions from their correspondingly as-prepared solutions were studied at 298 K for 4 h using a clay dosage of 0.1 $\text{g}/50 \text{ mL}$ (solid:liquid) with keeping the operated pHs at the optimal values taken from Fe^{3+} adsorption studies onto the examined organo-clays, namely 2.8 for EDTA-B, and 3.2 for DMSO-B. The experimental adsorption procedure was conducted similar to that depicted in section 2.4.

The sorption kinetics for the removal of Mg^{2+} , Ca^{2+} , and Sr^{2+} from artificially produced water were carried out using the most efficient organoclay at its corresponding optimal pH and at 298 K. The remaining experimental conditions were the same as above described. After an appropriate time interval (in the range 8–100 min), 0.02 mL of the mixed solution was withdrawn for analysis of the examined scaling cation using ICP-MS, taken as the average of triplet measurements. The obtained sorption kinetic data were investigated by applying the pseudo-second-order, Fickian diffusion and Elovich models [50,51], as being described in section 2.4.2.

2.6. Experimental pilot plant set-up for treatment of oilfield produced water: sorbent regeneration and corrosion studies

The pilot experiment used in this study (Fig. 2) was seemingly planned to simulate the industrial operating conditions in the Abu-Rudeis oilfield. A sedimentation tank (500 mm × 1,500 mm × 2,000 mm) of effective volume 1.3 m^3 was charged with produced water collected from the upstream pipelines of Abu-Rudeis oilfield, for instance, the OPW was supplied from sampling no. 2 (Table 1). The supernatant in this tank was monthly pumped into a feed tank (200 mm × 300 mm × 400 mm, effective volume 400 L), occupying it by 216 L (Fig. 2). These tanks were reinforced concrete structure coated with waterproof mortar inside and merely filled to 50% of their volume. Glass fiber reinforced plastic discs (Flow Ezy Filters, Inc. M 20 6, USA) of 10 mm diameter with 50 mesh size screen was employed to reduce suspensions in the OPW. A stream of OPW was pumped from the feed tank to a constant flow stirred tank reactor (CFSTR), which was fully occupied by 0.5 L, using a peristaltic pump (Masterflex L/S, Cole-Parmer Instrument Co., QC), adopting a flow rate of 100 mL/min at ambient temperature, Fig. 2.

For a fundamental pilot experiment, the proper amount of the most found efficient organo-modified clay adsorbent (10 g) was suspended in the oilfield produced water

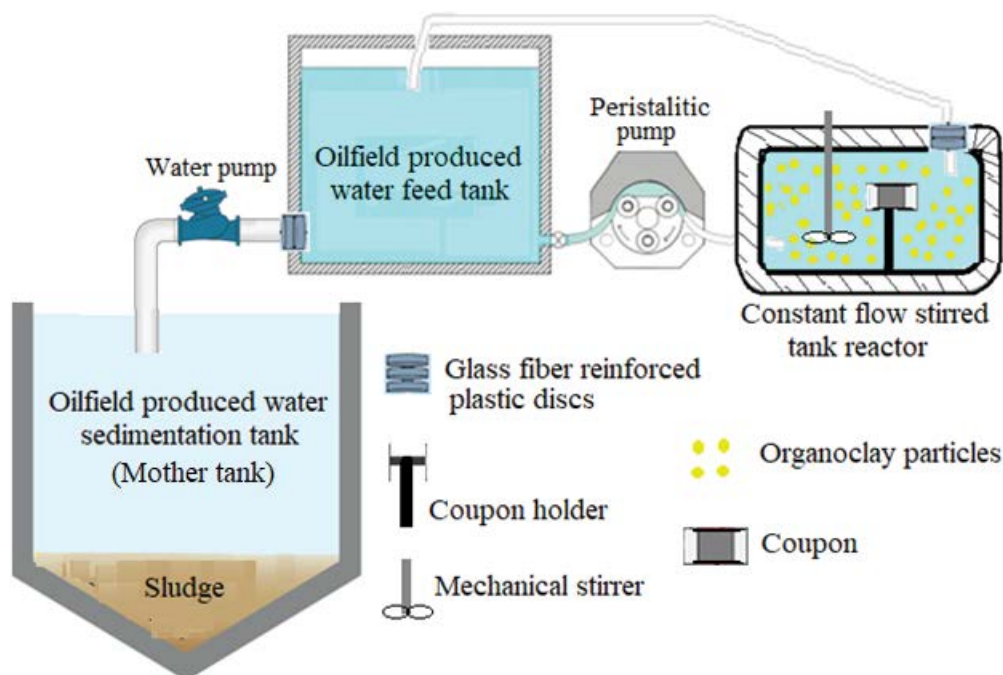


Fig. 2. Schematic diagram of the experimental pilot plant set-up.

inside CFSTR for removal of scale-forming cations. Glass-reinforced disc filters were used to maintain the organoclay particles in the CFSTR and improve the water quality of the influent, which was returned back to the feed tank for further treatment cycle (Fig. 2). As the CFSTR possessed a space-time of 5 min, all the produced water in the feed tank (216 L) had been undertreated by organoclay suspension with 20 cycles per month. By completing a one-month OPW purification run, the treated OPW was removed from the feed tank to analyze the concentrations of Fe^{3+} , Mg^{2+} , Ca^{2+} , and Sr^{2+} cations and detect their corresponding removal performances (%). The spent organoclay particles were filtered out from the CFSTR suspension and regenerated by soaking the spent organoclay in 250 mL solution of 0.5 M HCl for 16 h at 65°C to remove any adsorbed metal ion species from the clay lamellar structure [18,51]. The obtained solid fractions were centrifuged, washed with deionized water several times, and then dried at 110°C for 4 h. Afterward, the regenerated organoclay samples were reused for new adsorption of scaling cations from oilfield produced water in a second purification run via pumping up another 216 L from the supernatant of the mother tank into the feed tank, where OPW treatment was carried out following the afore-said procedure. The OPW purification runs were repeated for a further 4 months with conducting the regeneration/reusing process of the spent organoclay adsorbent as well as the quantitative analysis of the scale-forming cations in the treated-OPW after each run. The regenerated organoclay adsorbent used in the sixth OPW purification run and its correspondingly spent adsorbent form, which was collected at the end of such run, were analyzed using FTIR spectrometer.

In a preliminary study of the corrosion protection of the most found efficient organo-modified clay adsorbent,

namely EDTA-B organoclay, to steel pipeline structure, the corrosion feature of X-70 steel, which was commonly used in Egyptian petroleum companies, was examined by holding coupon in the fundamental pilot experiment, Fig. 2. The coupon used was supplied by X-70 steel from Abu-Rudeis oilfield pipelines, South Sinai, Egypt, with a chemical composition (wt.%) of C 0.058, Mn 0.093, Si 0.001, Ni 0.017, Cr 0.018, Mo 0.018, Cu 0.141, V 0.016 and the balance Fe. Coupon with the dimensions of 50 mm × 50 mm × 20 mm were machined (without polishing), degreased in acetone, washed with ethanol, and then sanitized under a UV lamp for 30 min before being immersed in the examined organoclay suspension in CFSTR for subsequent 6 purification runs along half a year. At the end of the six-month immersion period, the tested coupon was washed in running water, ultrasonically cleaned in methanol for 15 min and then dried at 50°C under vacuum. A blank comparative experiment took place in which the X-70 steel coupon was exposed to OPW flow with a rate of 100 mL/min at ambient temperature for continual six months in absence of organoclay suspension. To gain a generic insight into the corrosion protecting behavior of the examined organoclay (namely, EDTA-B) to steel structure, a detailed scaling description of the obtained coupons from the blank and fundamental experiments were given-up by scanning electron microscopy (SEM, of model JEOL-JSM T2000, the camera of model JEOL-T20-CSI) and XRD studies. A high-resolution camera was also used for visual inspection of the corroded specimens.

Moreover, the corrosivity of the obtained OPW from blank and fundamental experiments were preliminarily studied via determining Langelier saturation index (LSI), as described elsewhere [14]. For supporting the corrosion results, the mass loss decreasing rate (MLDR) was taken

to indicate the improved level of corrosion resistance, and the calculation formula was expressed as:

$$MLDR = \frac{ML_{\text{blank}} - ML_{\text{fundamental}}}{ML_{\text{blank}}} \times 100 \quad (14)$$

where, ML_{blank} and $ML_{\text{fundamental}}$ belonged to the mass loss percentage of the tested coupons in the blank and fundamental experiments, respectively [9].

2.7. SRB cultivation and cell enumeration: biocidal activity of clay samples understudy

The SRB seed was isolated from Abu-Rudeis oilfield from sample no. 2 (Table 1). It was indexed as *Desulfotomaculum nigrificans* [52]. It was cultivated in a culture medium for SRB at 37°C for 24 h before use. The composition of the SRB culture medium was (g/L): K_2HPO_4 0.01, $MgSO_4$ 0.2, $(NH_4)_2Fe(SO_4)_2$ 0.2, NaCl 10, yeast extract 1.0, vitamin C 0.10, sodium lactate 4 (pH 7.2). The culture medium and Abu-Rudeis oilfield produced water were sterilized, individually, in an autoclave for 20 min at 120°C, and then deoxygenated by sparging high-purity nitrogen gas.

In each 10 mL anaerobic tube, 0.1 mL of SRB seed culture was mixed with a suspension of Abu-Rudeis oilfield produced water (9.9 mL), which was inoculated by 0.1 g of the tested clay sample at a concentration of 1% (w/w). This tube was anaerobically incubated at 37°C for 20 d, and the most probable number method (MPN, cells/mL) was managed to enumerate planktonic and sessile SRB cell counts using an SRB culture medium as reported elsewhere [52,53]. To ensure the accuracy of the results, three replicate samples were used for SRB cell counting for each experimental system. To assess the biocidal activity of the tested organoclay against SRB, a control experiment based on mixing SRB seed culture with supernatant OPW was performed, as being described below:

$$\text{Biocidal activity (BA, \%)} = \left(\frac{MPN_0 - MPN_T}{MPN_0} \right) \times 100 \quad (15)$$

where MPN_0 and MPN_T were the cell numbers of SRB species in the seed culture in the absence and presence of the tested clay sample, respectively.

3. Results and discussion

3.1. Characterization of acid-treated and organically modified clay samples

3.1.1. Structural study

The XRD patterns of acid-treated reference clay and its derivatives are presented in Fig. 3a. The diffractogram of the acid-treated Egyptian clay (R-B) generally shows basal (001) and (002) reflections at 2θ -8.75° and 12.70°, respectively, indicating the presence of the interlayer basal space characteristic to bentonite clay [29]. The $k \neq 3n$ reflections of hk indices of (02-), (11-), (13-), and (20-) reflects the

presence of slightly deformed and randomly stacked layers in bentonite structure [30]. A sharp peak at $2\theta = 26.80^\circ$ indicates the reflection of (101) plane of OCT (opal-CT as para-crystalline silica, $SiO_2 \cdot H_2O$) [29]. Upon modification of R-B bentonite clay by EDTA, the 2θ basal (001) reflection is delayed from 8.75° to 6.67° linked with a marked increase in the d_{001} basal spacing from 0.7 to 1.3 nm (Fig. 3a). This accentuates the efficient intercalation of EDTA molecules inside the clay interlamellar spaces. By modifying R-B bentonite clay with DMSO, the crystallinity and interlamellar structure of R-B clay are markedly deteriorated, resulting in the disappearance of the clay characteristic basal (001) and (002) reflections. From this consideration, it is clearly evident that modifying the clay sheets by DMSO molecules forms probably a featureless XRD pattern in concert with the clay exfoliating aspect.

The FTIR spectra of R-B and various understudied organoclays (EDTA-B and DMSO-B) are depicted in Fig. 3b. The FTIR spectrum of R-B anticipates the existence of bentonite as the dominant mineral phase. The strong absorption bands in the 1,000–1,200 cm^{-1} region belong to the stretching vibrations of Si–O groups in the silicate structure [28]. The FTIR bands at 620, 698, and 905 cm^{-1} are attributed to Si–O–Al, Si–O–Si_{out-of-plane} and Al–OH bending vibrations, respectively [30,32]. An intense absorption band relating to the absorbed water molecules appears at 1,630 cm^{-1} [28]. A strong, broadband in the range from 3,000 to 3,700 cm^{-1} is assigned to the stretching vibrations of silanol OH groups [28]. The sharp absorption band at 790 cm^{-1} reflects stretching vibrations of Si–O in paracrystalline silica [28].

Upon modification of R-B bentonite clay by EDTA, new peaks characteristic to EDTA molecules appear at 1,563; 1,715; and 2,925 cm^{-1} describing the stretching vibrations of deprotonated carboxylic acid ($-COO^-$), $-COOH$, and $-CH_2$ group, respectively [35,40]. Some of the characteristic peaks of R-B are red-shifted, as the absorption bands belonged to Si–O–Al, Si–O–Si_{out-of-plane} and Al–OH bending vibrations record intensities at 535, 605, and 875 cm^{-1} , respectively (Fig. 3b). These findings presumably reflect the preferential linkage of carboxylic species of EDTA ($-COOH$) to the siloxane oxygens and aluminols via hydrogen bonding. Such EDTA-clay interactions facilitate intercalation and occupation of EDTA molecules to the clay interlamellar spaces.

By modifying R-B bentonite clay with DMSO, a marked decrement in the intensity of siloxanes (Si–O–Si) stretching vibration band is observed linked to the disappearance of the bending vibrations of Si–O–Al, Si–O–Si_{out-of-plane} (Fig. 3b). It is worthy to attribute these results to the oxidant character of DMSO molecules that break up the bonding network in the clay structure (Si–O–Si and Si–O–Al oxygen bridges), following the same line of discussion in previous researches that served DMSO as an efficient oxidizer by giving it is sulfinyl oxygen atom ($-S=O$) to the siloxane bridges (Si–O–Si) yielding non-bridging oxygen species (NBO), [54,55]. As presented by Kagan et al. [54], the formed NBO generally acquire more stability by being protonated by a nearby physisorbed water molecule to produce silanols and aluminols at the location of the NBO. As seen from Fig. 3b, highly significant lowering in the frequencies of aluminols ($\gamma_{Al-OH} = 820 \text{ cm}^{-1}$) and silanols ($\gamma_{Si-OH} = 3,050 \text{ cm}^{-1}$) are also observed, revealing most probably the

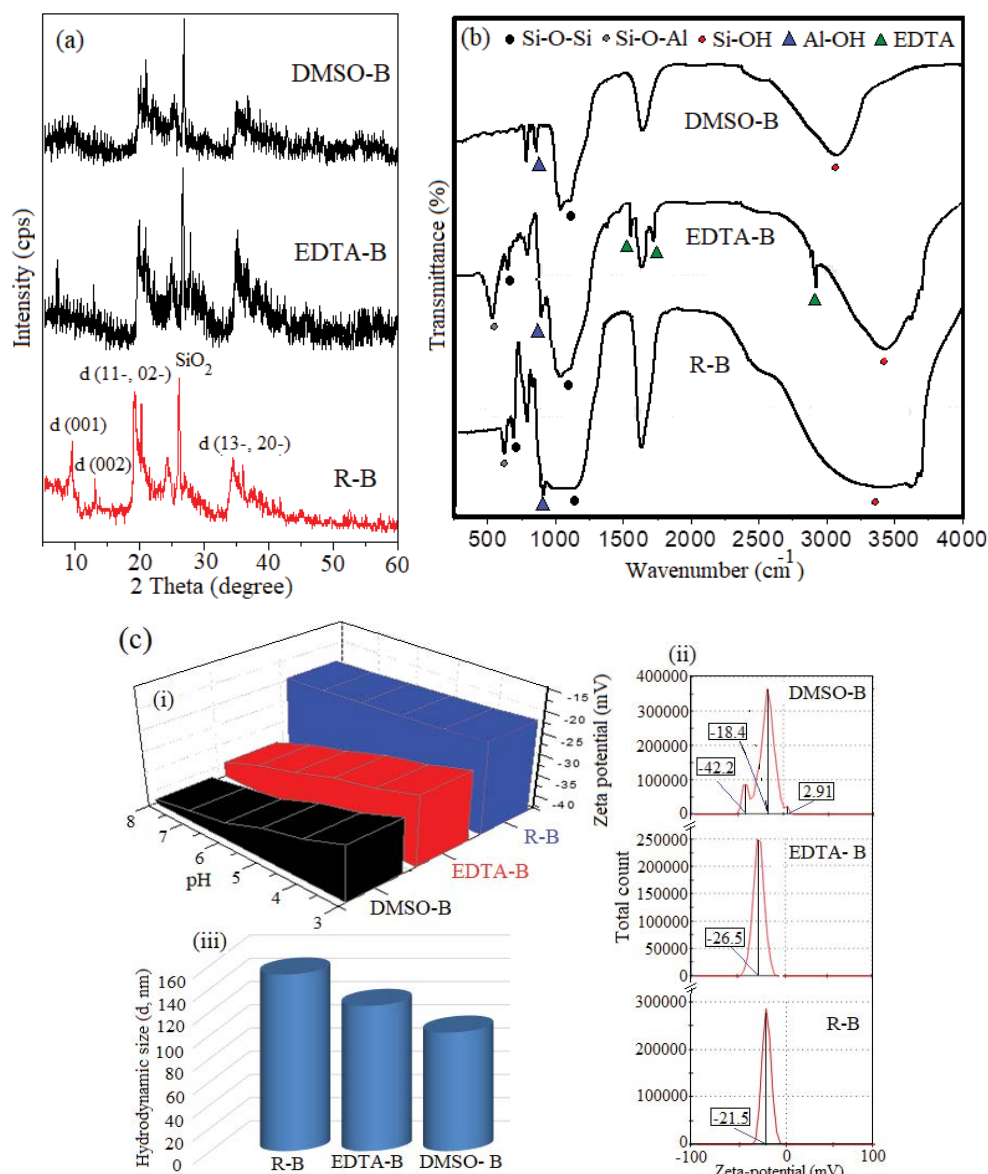


Fig. 3. XRD patterns (a), FTIR spectra (b), and hydrodynamic correlations (c) of the clays under study.

capability of sulfoxide groups ($-S=O$) of DMSO molecule to hydrogen bond with the produced silanols ($-SiOH$) and aluminols ($-AlOH$) in the clay galleries. This explanation is complying with previous works that consider DMSO as a good hydrogen bond acceptor [37,39]. In this respect, the sulfoxide group ($S=O$) seems to be the key point behind the severe attacking of DMSO molecules to the clay sheet structure and the marked deterioration in the clay lamellar behavior; a fact that strongly serves DMSO as a clay exfoliator.

3.1.2. Surface charges and textural studies

The obtained surface charges, governed by zeta-potential, as well as the hydrodynamic particle size measurements of R-B, EDTA-B, and DMSO-B clay samples, are depicted in Fig. 3c. As clearly shown, the measured ζ -potentials

as a function of pH in the 3–8 range is highly negative (between -20 and -45 mV) with an unattainable isoelectric point (Fig. 3c,i), referring mostly to the excessive presence of deprotonated silanols ($Si-O^-$) even in the highly acidic medium. Comparing to the ζ -potentials of reference R-B sample, EDTA-B and DMSO-B organoclays record higher negatively charged ζ -values, over the whole pH range studied, pointing most probable to the beneficial role of the deprotonated carboxylic species ($-COO^-$) of EDTA and the sulfoxide ($S=O$) groups of DMSO molecule in developing the surface charges of clay sheet structure. Interestingly, the increase in the negative charges of ζ -potentials by increasing the pH is much more pronounced for the DMSO-B clay sample rather than for EDTA-B, achieving ~ -45 mV at pH 9, Fig. 3c,i. This phenomenon may reflect the greater affinity of the sulfoxide group to degenerate oxygen bridges in the clay sheet structure forming copious of silanols and

aluminol species of remarkable negatively charged ζ -potentials, particularly in the alkaline medium, *cf.* FTIR results.

For more assessment of the surface charge characteristics of the under-investigated clay samples, ζ -potential distribution curves are managed (at pH 3.0) to demonstrate the average zeta-potentials (ζ_{av}), as shown in Fig. 3c,ii. The R-B clay sample displays a sharp peak at $\zeta_{av} = -21.5$ mV, reflecting the presence of stabilized negatively charged particles [51]. For EDTA-B particles, the net negative charges (between -10 and -50 mV) is ameliorated affording a unimodal ζ -potential distribution curve of $\zeta_{av} = -26.5$ mV, thus assures the adequate power of carboxylic species (COO^-) of EDTA to stabilize the clay particles. In the case of DMSO-B, the ζ -potential distribution curve adopts a tri-modal charged system of diverse ζ_{av} potentials at -42.2 , -18.4 , and $+2.9$ mV (Fig. 3c,ii). Such diversity in ζ_{av} values may refer to the rage of the sulfoxide group to fracture the clay lamellar structure serving several surface fractions with different charging properties, as evidenced by XRD and FTIR studies. The obtained results are more confirmed by estimating the average hydrodynamic particle size of the as-prepared clay samples, Fig. 3c,iii. It deserves to be mentioned that increase in the negativity of ζ_{av} values from R-B to EDTA-B to DMSO-B clay samples results in a pronounced reduction to their corresponding average hydrodynamic particle size from 154 to 105 to 86 nm, respectively, *cf.* Fig. 3c,iii.

Textural characteristics of R-B, EDTA-B, and DMSO-B clay samples are recognized by the aid of N_2 adsorption-desorption isotherms (Fig. 4a). It is clearly discernable that all the isotherms are of type II per International Union of Pure and Applied Chemistry classification linked with a closed H3 type hysteresis loop at $P/P_0 \sim 0.45$ for R-B and EDTA-B clay samples, accentuating the presence of mainly mesoporous solids of agglomerated particles enriched by slit-shaped pores [43,45]. However, for DMSO-B, the obtained isotherm seems to be completely reversible inferring most probably the evolution of large-sized mesoporous solid fractions, which limit from the capillary condensation phenomenon.

The different surface parameters derived from adsorption-desorption isotherms are summarized in Table 2. The specific surface areas (S_{BET} , $\text{m}^2 \text{g}^{-1}$) are derived from the linear relation of Brunauer-Emmett-Teller (BET) [43]. The total pore volumes (V_p , mL g^{-1}) are estimated from the amount of N_2 adsorbed at $0.99 P/P_0$ [43], and the average pore radii (r_p , \AA) are calculated following the slit-shaped pore model described elsewhere [28,45]. The most abundant hydraulic pore radii (\bar{r}_h , \AA) are detected from pore size distribution (PSD) curves (Fig. 4b) using Barrett-Joyner-Halenda method from the desorption branch of the isotherm [45].

It can be seen from Table 2 that the treatment of R-B bentonite clay with EDTA causes a two-fold reduction in the surface area (from 42 to $19 \text{ m}^2 \text{g}^{-1}$) and V_p values (from 0.0875 to 0.0442 mL g^{-1}). This is associated with a marked increase in pore size and pore uniformity, namely, r_p (from 40 to 48 \AA) and \bar{r}_h (from an uneven bimodal PSD of pore fractions at 17 and 30 \AA to a sharp unimodal PSD of 24 \AA in size), Fig. 4b. These results reveal most probably the capability of EDTA molecules to move freely all over the clay interlayer spaces going along different ways; either to be located beyond the lamellar edges and/or intercalated within the clay galleries. In the case of DMSO-B, dramatic depression in the surface area and total pore volume are observed, when compared with R-B surface parameters (Table 2). However, the pore sizes of DMSO-B are highly extended compared to those of R-B yielding r_p of 87 \AA linked with the existence of non-uniform bimodal PSD, where broader and less intense pore fractions of $\bar{r}_h = 20$ and 92 \AA can be detected (Fig. 4b). Such results buttress the affinity of DMSO molecule, as an oxidant and a good hydrogen bond acceptor [37,54], to tentatively interact with the laminated clay sheets and markedly straggle the stacking order of clay layers creating clay particles of poor surface properties.

3.1.3. Morphological study

Studying the morphological properties of the under-investigated clay samples by AFM technique may be the

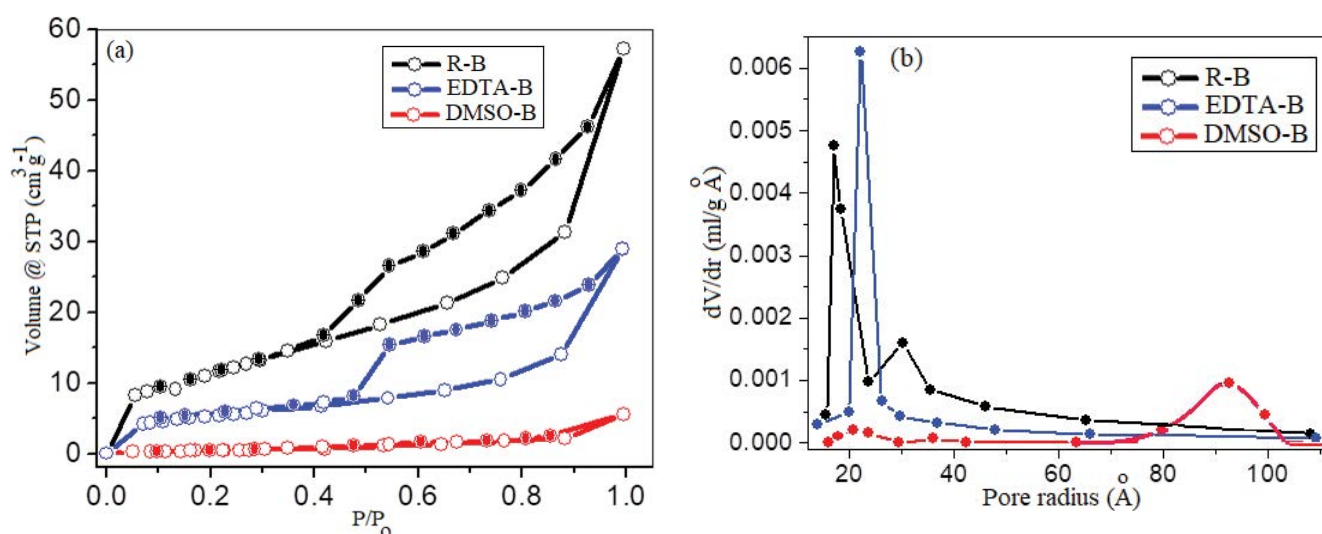


Fig. 4. N_2 adsorption-desorption isotherms (a) and pore size distribution curves (b) of clays under study.

Table 2
Textural parameters for clays under study

Samples	S_{BET} ($\text{m}^2 \text{g}^{-1}$)	V_p (mL g^{-1})	r_p (\AA)	\bar{r}_h (\AA)
R-B	42	0.0875	40	17–30 (bimodal system)
EDTA-B	19	0.0442	48	24 (unimodal system)
DMSO-B	2	0.0082	89	20–92 (bimodal system)

most likely way to bestow the influence of the used organo-modifiers on the lamellar structure of clay, as shown in Figs. 5a–c. The surface roughness in clay lamellae is quite demarcated in terms of the height in the z-dimension (Z) and quantitatively estimated depending on peak-to-valley distance ($P-V$), as being reported in previous works [51,56]. For reference R-B clay sample, extended uplifted lands are observed associated with the presence of sparse of rolled mountain peaks of $Z = 238 \text{ nm}$ and $P-V = 135 \text{ nm}$ (Fig. 5a). As seen from Fig. 5b, modifying the R-B sample by DMSO molecules causes pronounced deterioration in the clay lamellar structure affording much more roughened surfaces with an intensive number of shortened protrusions and hump-like zones of $Z = 137 \text{ nm}$ and $P-V = 72 \text{ nm}$, being close to half of those recorded for R-B. Such degenerative effect of DMSO molecules to clay lamellar structure may be caused by clay/sulfoxide intimate interactions, as being evidenced by the aforesaid structural and textural analyses.

On the contrary, modifying R-B clay by EDTA spectacularly enthuses the presence of large stacks of laminated clay layers, so-called “clay tactoids”, with preminent

heights ($Z = 1,189 \text{ nm}$ and $P-V = 446 \text{ nm}$). Furthermore, these clay tactoids seem to possess substantially flattened surfaces of extended widths ($\sim 1.0\text{--}2.0 \mu\text{m}$, pointed by yellow arrows in Fig. 5c), by which such tactoids may lean over each other in an oriented profile, *cf.* Fig. 5c. These results highly candidate EDTA to be an efficient intercalant to clay interlamellar spaces, encouraging compatibilization of clay layers to form highly oriented stacking tactoids. Such clay ordering perhaps results from the adequate established hydrogen bonding between the clay sheets and the protonated carboxylic species of EDTA molecules ($-\text{COOH}$), as being demonstrated from FTIR and ζ -potential studies.

For more clarification of the intense influence of DMSO and EDTA organic compounds toward the morphological feature of bentonite clay (R-B), HR-TEM investigation is performed as depicted in Figs. 6a–c. The representative image of R-B (Fig. 6a) implies the presence of compacted dimensionless lamellar clay patches. As can be seen from Fig. 6b, modifying R-B bentonite clay by DMSO results in pronounced deformation and delamination of clay structure, as shown from elements 1–4 in Fig. 6b,i. In Fig. 6b,ii,

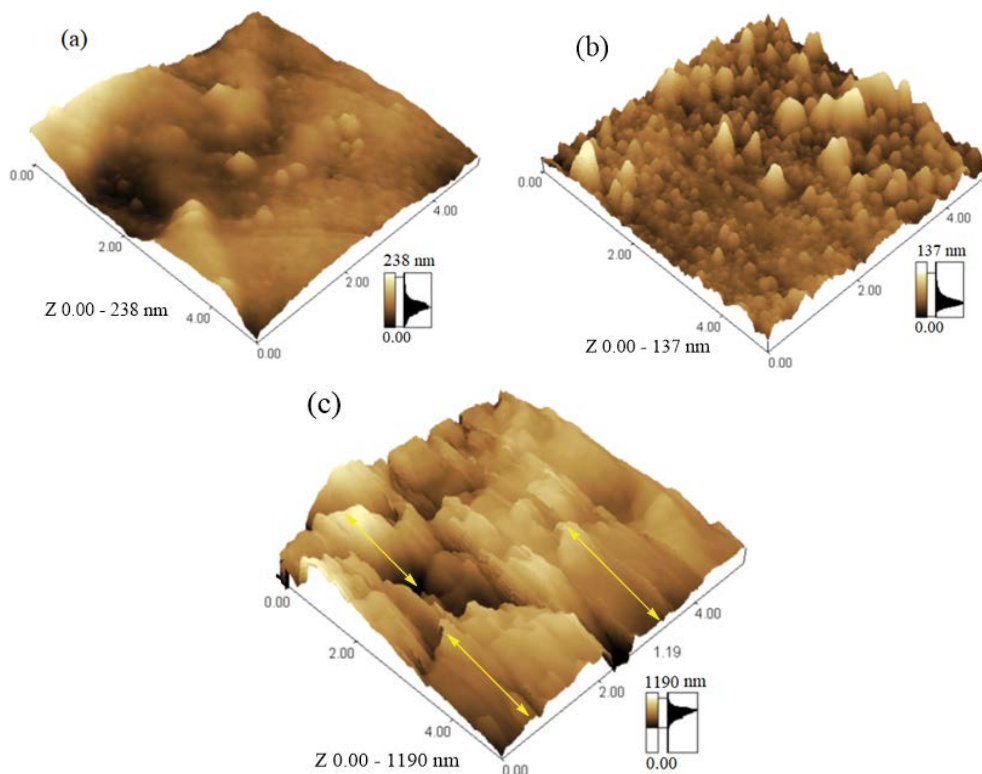


Fig. 5. Three-dimensional AFM topographic images of (a) R-B, (b) DMSO-B and (c) EDTA-B clay samples under study.

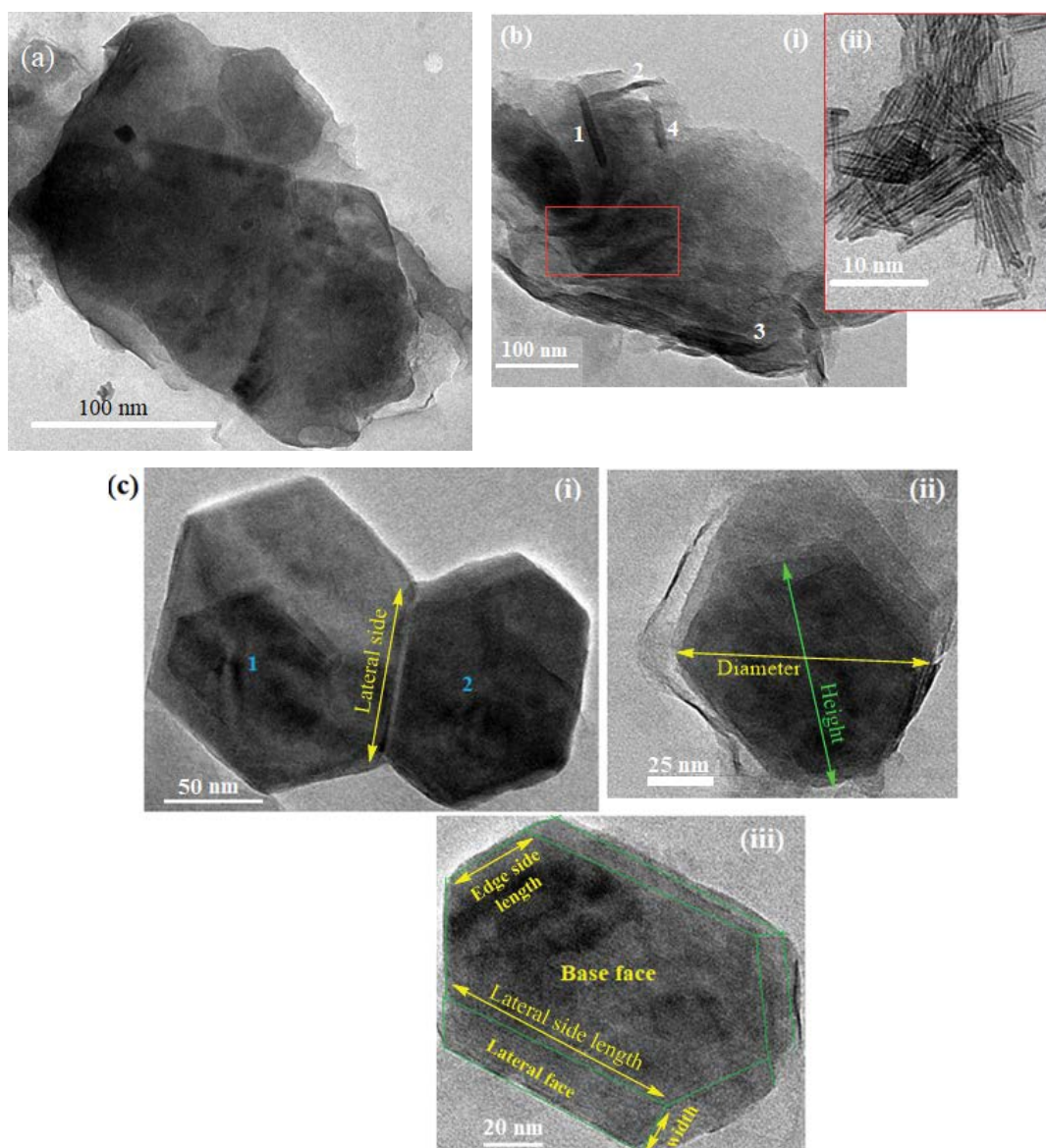


Fig. 6. HR-TEM micrographs of (a) R-B bentonite clay, (b) DMSO-B and (c) EDTA-B. The inset image shows an enlarged view of the organoclay under study.

the HR-TEM image magnifies the contents in the red solid area (Fig. 6b,i) pointing probably to the loss of the laminated structure of clay – a seminal case of exfoliation-linked with the presence of remarkable flocculated clay platelets. Such delamination seems to be attributable to the recommended intimate interaction between clay layers and sulf-oxide group (*cf.* XRD and FTIR results). On the other hand, modifying of R-B clay with EDTA creates a unique seriate order of hexagon-shaped stacks of clay lamellae (elements 1 and 2 in Fig. 6c,i), nominated by “clay tactoids”, that are interconnected from the lateral sides of *ca.* 82 nm length, as represented by the yellow arrow in Fig. 6c,i. Each clay tactoid seems to compose of a packet of inclined laminated clay layers of hexagon shape with a diameter (distance across corners) and height (distance across flats) in the vicinity of 95 and 85 nm, respectively, as represented by yellow

and green arrows in Fig. 6c,ii. It appears that the estimated lengths of the clay tactoids in the EDTA-B sample from TEM micrographs are much smaller than those detected by AFM analysis, which is registered to give images for large aggregates of multi-clay tactoidal systems. By catching a marginal scene to the clay tactoid by HR-TEM with higher magnification (Fig. 6c,iii), it seems to possess an oblique prism-like architecture encompassing hexagonal base faces of edge length ~ 32 nm, and rectangular lateral-side faces of width ~ 17 nm and length = 85 nm, as pointed by yellow arrows in image iii. Such conception of the structure of EDTA-B organoclay could presumably be attributed to the harmonic distribution of EDTA intercalant molecules inside the clay interlamellar spaces. Such beneficial distribution may arise from the suggested acceptable hydrogen bond linkages of protonated carboxylic species ($-\text{COOH}$) of EDTA

to siloxanes in the clay galleries, *cf.* FTIR and ζ -potential results.

3.2. Adsorption studies for removal of Fe^{3+} ions from artificially produced water by various clays under study

3.2.1. Effect of initial solution pH

Studying the influence of solution pHs, in the range of 1.8–3.4, onto the removal performances of the understudied clay systems is one of the most important landmarks in the pathway of sorption phenomenology of Fe^{3+} ions from artificially produced water. A series of batch equilibrium tests are carried out to recognize such pH influence and summarized in Fig. 7a. It is worth noting that modifying the R-B clay lamellar structure by EDTA and DMSO

molecules extend the working pHs to lower acidic ranges with shifting the optimal pH values from 2.0 to 2.8 to 3.2, respectively, where the removal performances are almost close to 90%. These findings are kindly attributed to the increased appeal to form silanols ($-\text{Si}-\text{OH}$), which are greatly runnable in the case of DMSO-B via clay exfoliation, being complied with XRD, FTIR, and ζ -potential results. These silanol groups encourage ion-dipole interactions with the positively charged adsorbate ions like Fe^{3+} [28,54].

3.2.2. Adsorption equilibrium studies

The isothermal relationships between the equilibrium concentrations of Fe^{3+} in the solid and the liquid phases (q_e vs. C_e) for R-B, DMSO-B, and EDTA-B clays at their corresponding optimal pHs are shown in Fig. 7b. The isotherm

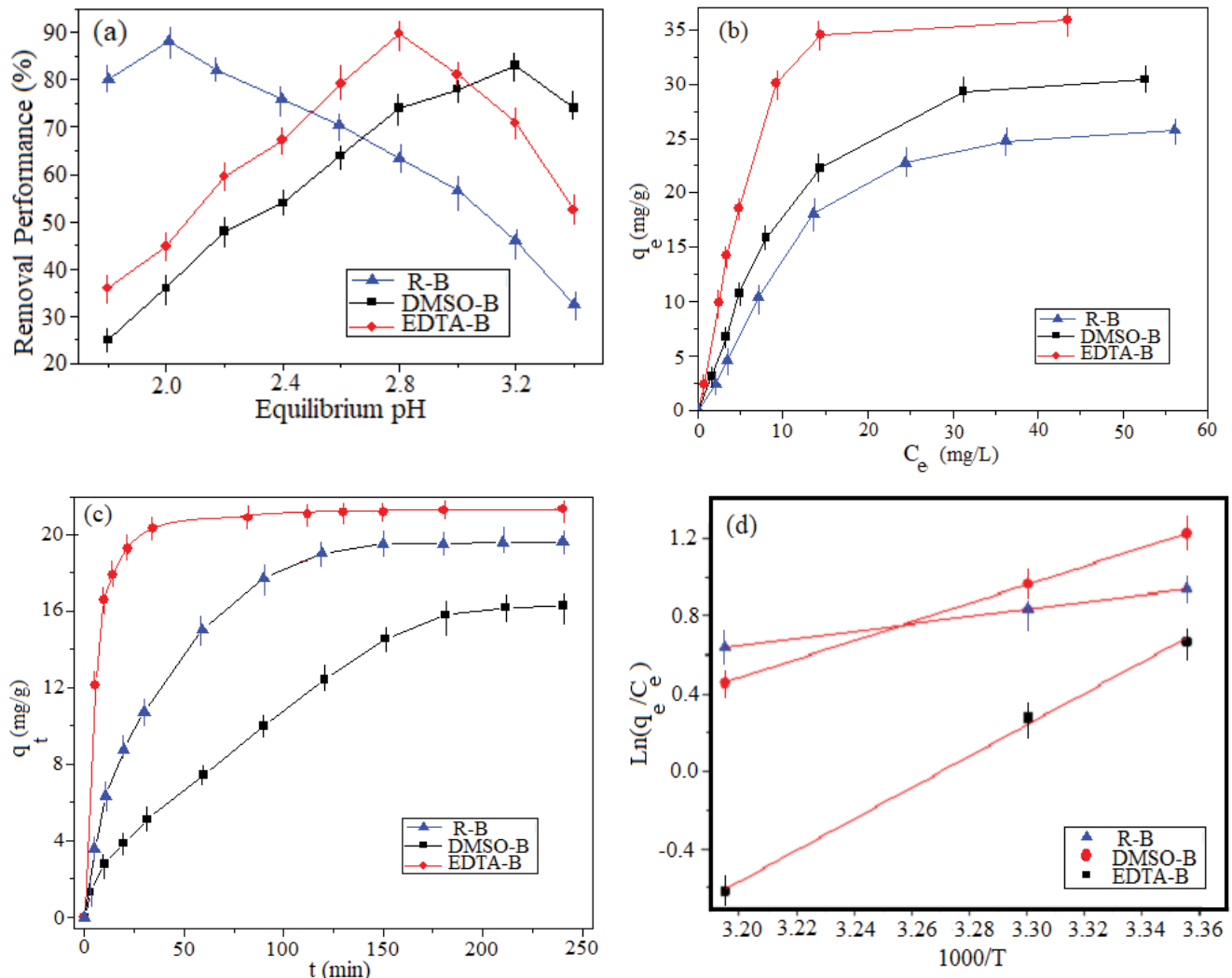


Fig. 7. The uptake studies for removal of Fe^{3+} from artificial produced water by various understudied clay samples applying (a) effect of solution pH (clay content: 2 g/L; initial iron ion concentrations: 50 mg/L; temperature: 298 K; time: 4 h), (b) adsorption equilibrium isotherms (pH: R-B 2.0; DMSO-B: 3.2; EDTA: 2.8; clay content: 2 g/L; initial iron ion concentrations: 10, 20, 40, 50, 70, 90, 120 mg/L; temperature: 298 K; time: 4 h), (c) effect of contact time (pH: R-B 2.0; DMSO-B: 3.2; EDTA: 2.8; clay content: 2 g/L; initial iron ion concentrations: 50 mg/L; temperature: 298 K), and (d) thermodynamic analysis (pH: R-B 2.0; DMSO-B: 3.2; EDTA: 2.8; clay content: 2 g/L; initial iron ion concentrations: 50 mg/L; time: 4 h).

plots clearly show that the organoclays have much higher adsorption capacity compared to reference R-B clay, often of Fe^{3+} uptake capability in the order EDTA-B > DMSO-B (Fig. 7b). This possibly reflects what extent alteration in the clay lamellar structure can deeply affect the adsorption progression of iron ions from aqueous solution, taking into consideration the chief role of the ordered clay lamellar stacking model (Fig. 6c) to uphold the intercalant EDTA molecules and accommodate sites of increasing adsorption affinity toward Fe^{3+} ions, mainly the oxygen bridges in clay structure and the deprotonated EDTA carboxylic species ($-\text{COO}^-$). Accordingly, the EDTA-B sample, thereby its distinct maximum amount of Fe^{3+} adsorbed ($q_e = 37 \text{ mg/g}$), perhaps stands in competition with most of the existing adsorbents in literature like ion-exchange resin, clays, chitosan, and carbon nanotube [56–58] that registered equilibrium adsorption capacities of at most 45 mg/g. But, an inspection of the literature, it was exceptional for the chitosan/resin composites which showed superior Fe^{3+} adsorption capacity values at equilibrium, exceeding that recorded using EDTA-B by at least two times [59,60].

Adsorption models, including Freundlich, Langmuir, Dubinin–Radushkevich, and Temkin, are examined to the obtained adsorption isotherms for clays under study. The derived adsorption isotherm plots and coefficients are summarized in Fig. S1 and Table 3, respectively. Freundlich isotherm best describes the Fe^{3+} uptake by R-B and DMSO-B with $r^2 \sim 0.98$. This suggests that adsorption is not onto a uniform site rather multilayer adsorption occurred on heterogeneous surfaces of R-B and DMSO-B clay systems, where doubled privilege to the adsorption capacity of DMSO-B (of $K_F = 2.31 \text{ mg}^{1-1/n} \text{ L}^{1/n} \text{ g}^{-1}$) is observed. However, monolayer adsorption seems also to play a very important role in the Fe^{3+} uptake onto the all understudied clay samples, being attributed to the better-fitting of Langmuir isotherm plots, Table 3 and Fig. S1. This confirms the embracement of clay lamellar surfaces to homogeneous adsorption sites, which become highly dominant and energetic in the EDTA-B clay system, yielding $K_L = 27.6$ of nearly three times and half that detected from DMSO-B, cf. Table 3. The calculated R_L values (from linear Langmuir isotherm) of the under-investigated clays are almost less than the unity favoring the existence of adsorption processes [60].

The experimental adsorption isotherm data are quietly fitted to the D–R model with $r^2 \geq 0.96$. The theoretical adsorption saturation capacity (q_D , mg/g) of the as-prepared clays drawn from the D–R isotherm equation (Table 3) are complying with that measured from

equilibrium adsorption isotherms (Fig. 7b) confirming the applicability of D–R model to describe the adsorption progress. The adsorption energy (E) and q_D values in terms of adsorbent nature increase as R-B < DMSO-B < EDTA-B, reflecting a sequential increment in the binding of Fe^{3+} ions to the adsorption sites of EDTA-B organoclay lamellar structure. As the highest recorded E value does not exceed 5 kJ/mol, the Fe^{3+} -clay interaction is most probable controlled by physical forces (non-covalent interactions) [51], achieving the highest strength often when the deprotonated carboxylic species (COO^-) of EDTA-B is electrostatically bonded to Fe^{3+} ions. This emphasizes the elevated q_D value obtained from the EDTA-B clay sample.

Further studying on the adsorption isotherm models of the clays under investigation is provided by applying the Temkin plot (Fig. S1). It is worth mentioning that the Temkin adsorption model is an excellent fit to R-B and DMSO-B clay samples (of $r^2 \sim 0.99$) and yields coefficients (K_T) of 45.6 and 64.2 L/g, respectively, corroborating the presence of heterogeneous-type interactions with a privileged approach for adsorbate/adsorbate binding that suits best in DMSO-B (Table 3).

3.2.3. Kinetic and thermodynamic studies

Interpreting the rate and the detailed mechanism of the adsorption process can be strongly ensued by studying the adsorption of Fe^{3+} onto R-B, DMSO-B, and EDTA-B clays as a function of time at initial iron(III) concentration of 50 mg/L and temperature 298 K, as shown in Fig. 7c. Clearly, the equilibrium time is reached after approximately 170 min for both R-B and DMSO-B samples following a gradual increase in the amount of metal ion adsorbed, where the equilibrium adsorption capacity of R-B is nearly increased 20% over that of DMSO, Fig. 7c. Meanwhile, the initial adsorption of Fe^{3+} ions onto EDTA-B is very fast and the maximum uptake is recorded within ca. 20 min. The kinetic curves in Fig. 7c are treated according to pseudo-first-order, pseudo-second-order, Fickian, and Elovich models, Fig. S2. The derived adsorption kinetic parameters are illustrated in Table 4. A comparison of the correlation coefficients (r^2) between pseudo-first and second-order models shows that the adsorption mechanism is satisfactorily explained by a pseudo-second-order process in all the understudied clays, implying dependence of Fe^{3+} adsorption on both metal ions concentration and physicochemical feature of the modified clay sorbent (Table 4). EDTA-B clay sample displays the highest adsorption rate of tenfold increment

Table 3

Freundlich, Langmuir, Dubinin–Radushkevich and Temkin coefficients for Fe^{3+} removal from artificially produced water using various understudied clay samples (pH: R-B 2.0; DMSO-B: 3.2; EDTA: 2.8; clay content: 2 g/L; initial iron ion concentrations: 10, 20, 40, 50, 70, 90, 120 mg/L; temperature: 298 K; contact equilibrium time: 4 h)

Sorbents	Freundlich model		Langmuir model			Dubinin–Radushkevich model			Temkin model	
	K_F ($\text{mg}^{1-1/n} \text{ L}^{1/n} \text{ g}^{-1}$)	r^2	$K_L \times 10^2$ (L mg^{-1})	r^2	R_L	q_D (mg g^{-1})	E (kJ mol^{-1})	r^2	$K_T \times 10^2$ (L g^{-1})	r^2
R-B	1.30	0.98	5.3	0.95	$0 < R_L < 1$	23.2	2.63	0.97	45.6	0.98
DMSO-B	2.31	0.98	7.9	0.99	$0 < R_L < 1$	27.3	3.00	0.96	64.2	0.99
EDTA-B	4.66	0.92	27.6	0.98	$0 < R_L < 1$	36.4	3.78	0.98	39.8	0.76

to those obtained by R-B and DMSO-B samples, reflecting the efficient adsorption capacity of EDTA-B for iron ions. As seen from Table 4, all the understudied clay samples likely follow Fickian diffusion law and Elovich kinetic model plotting regression lines of near unity r^2 values. Based on these facts, there is a possibility of diffusion of Fe^{3+} species within the interior parts of the clay pore structure by keeping most of the metal ions physisorbed to energetically active sites on the internal surfaces of clay. The negative values of X (Table 4) indicate no boundary layer effect on the rate of adsorption allowing intraparticle diffusion to be the sole rate-limiting step [56]. Obviously, the Fe^{3+} ions are found to have a preeminent tendency to be adsorbed onto EDTA-B than over DMSO-B and R-B clay samples yielding an intraparticle diffusion rate constant (k_i) of $6.41 \text{ mg g}^{-1} \text{ min}^{-0.5}$ and an initial adsorption rate constant (α) of $6.72 \text{ mg g}^{-1} \text{ min}^{-1}$, Table 4. Meanwhile, DMSO-B shows the poorest adsorption kinetic constants reflecting precedence toward the existence of low-energy adsorption sites in the clay gallery.

Comparing with the previously presented reports in the literature, the EDTA-B clay sample conducts the highest ever seen kinetic parameter values in the literature for Fe^{3+} adsorption [57–60]. This fact confirms possession of EDTA-B to the flux of highly energetic and efficient adsorption sites for iron ions than any other tested clay sample. The outstanding adsorption behavior of EDTA-B is congruent to the results obtained from Langmuir and D–R isotherm models.

For further assessment of the interacting modes proceeded in the clay samples under investigation, thermodynamic parameters including enthalpy (ΔH°), entropy (ΔS°), and free energy (ΔG°) changes are detected and illustrated in Table 4. All the understudied clay systems exhibit negative ΔH° and ΔS° values, suggesting that the adsorption process is exothermic in nature with decreased attitude in the randomness at the solid–liquid interface during the adsorption of Fe^{3+} onto clay surfaces. The obtained values of ΔG° are in between -1.77 and $-3.17 \text{ kJ/mol}^{-1}$ (Table 4), reflecting the spontaneity of the adsorption process and the existence of non-covalent interactions between Fe^+ ions and various organoclays under study. The moderated thermodynamic values obtained from Fe^{3+} adsorption onto DMSO-B anticipates the presence of barely energetic sites capable to link with iron(III) ions through main silanols just adopting ion-dipole interactions. As can be deduced from Fig. 7d and Table 4, the EDTA-B sample records ΔH° and ΔS° thermodynamic values far greater than those of DMSO-B clay, a fact that endorse the establishment of stronger iron(III)-organoclay interactions, affording a large contribution to the coulombic forces between Fe^{3+} ions and EDTA carboxylate anions (COO^-) accompanied by limited cooperation to the ion-dipole forces between Fe^{3+} and siloxane bridges. Such interacting mode serves a significant adsorption exothermicity with a highly ordered Fe^{3+} uptake profile.

3.2.4. Mechanism modeling explanations for Fe^{3+} adsorption

On the basis of the all above-mentioned considerations to the physicochemical characteristics of DMSO-B and EDTA-B organoclays and their Fe^{3+} adsorption studies, the authors succeed to reshape the lamellar arrangement of Egyptian bentonite clay by the aid of commonly used organic

Table 4
Pseudo-first and second-order kinetics, and Fickian diffusion and Elovich model parameters for Fe^{3+} removal from artificially produced water using various understudied clay samples (pH: R-B 2.0; DMSO-B: 3.2; EDTA: 2.8; clay content: 2 g/L; initial iron ion concentrations: 50 mg/L; temperature: 298 K), and thermodynamic data for adsorption of $\text{Fe}(\text{III})$ on R-B, DMSO-B and EDTA-B (pH: R-B 2.0; DMSO-B: 3.2; EDTA: 2.8; clay content: 2 g/L; initial iron ion concentrations: 50 mg/L; contact time: 4 h)

Sorbents	Pseudo-first-order model		Pseudo-second-order model		Fickian diffusion model		Elovich model		Thermodynamic parameters			
	$k_1 \times 10^2$ (min^{-1})	r^2	$k_2 \times 10^3$ ($\text{g mg}^{-1} \text{min}^{-1}$)	r^2	$k_i \times 10^2$ ($\text{mg g}^{-1} \text{min}^{-0.5}$)	X	r^2	α ($\text{mg g}^{-1} \text{min}^{-1}$)	r^2	ΔH° (kJ mol^{-1})	ΔS° ($\text{kJ mol}^{-1} \text{K}^{-1}$)	ΔG° (kJ mol^{-1}) at 298 K
R-B	3.57	0.91	1.25	0.99	1.98	-0.57	0.99	1.48	0.99	-15.566	-0.044	-2.45
DMSO-B	1.95	0.81	0.17	0.96	1.41	-3.09	0.99	0.35	0.98	-39.830	-0.123	-3.17
EDTA-B	8.59	0.86	9.42	0.98	7.25	-5.46	0.98	6.26	0.98	-67.034	-0.219	-1.77

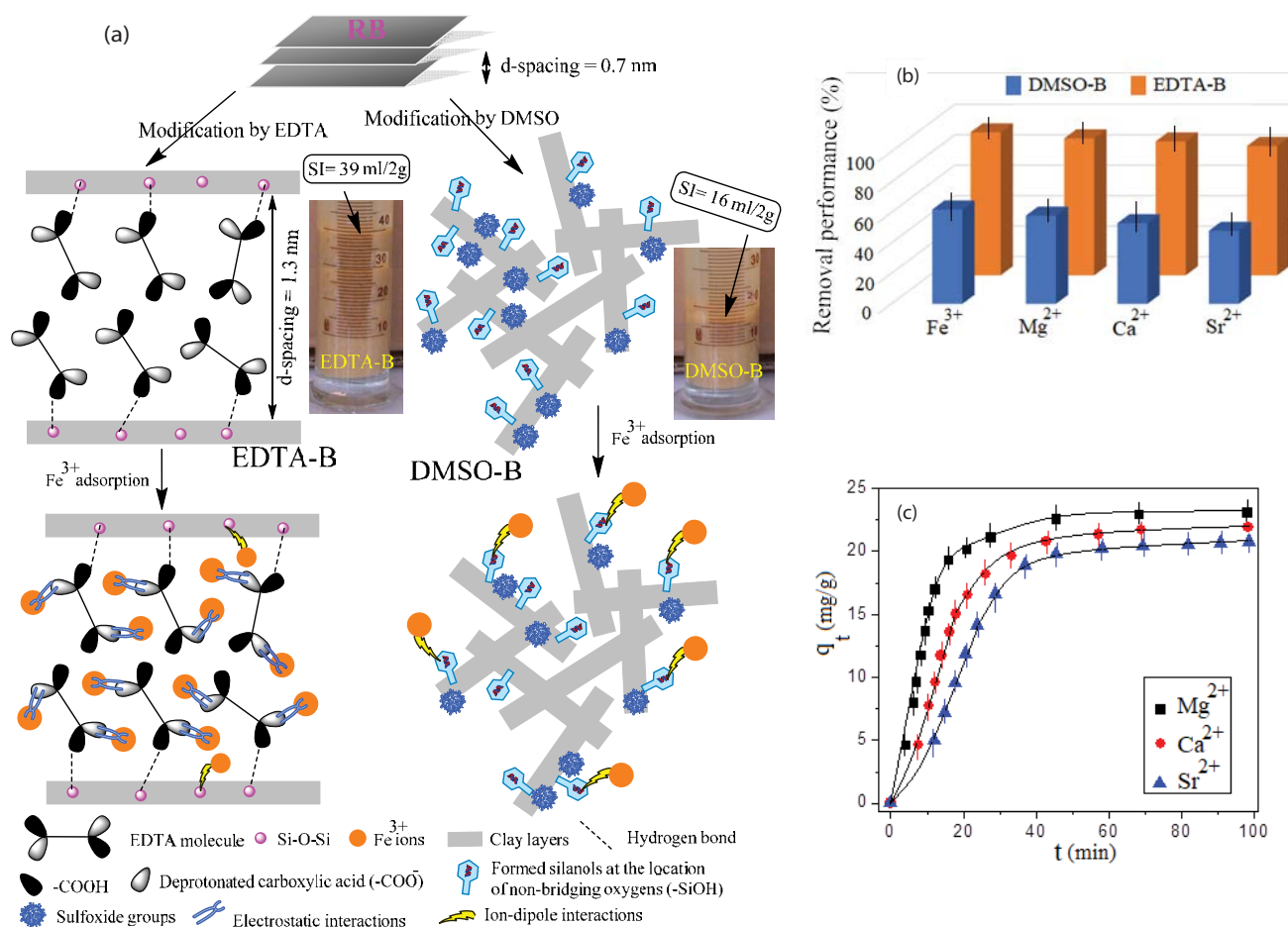


Fig. 8. (a) Schematic illustrations of the expected changes in clay lamellar structure as a function of the used organo-modifier and their interaction characteristics during Fe³⁺ adsorption from artificial produced water (The inset digital camera images show the swell index testing of organoclays under study), (b) removal performance of understudied organoclays for various scaling cations (pH: DMSO-B 3.2; EDTA: 2.8; clay content: 2 g/L; initial concentrations: Mg²⁺ 1,564 mg/L, Ca²⁺ 2,713 mg/L, Sr²⁺ 104 mg/L; 298 K; 4 h), and (c) kinetic studies for removal of scaling cations from produced water by EDTA-B (pH: 2.8; clay content: 2 g/L; initial concentrations: Mg²⁺ 1,564 mg/L, Ca²⁺ 2,713 mg/L, Sr²⁺ 104 mg/L; 298 K).

materials (like EDTA and DMSO) forming two entirely different clay layering profiles, giving the oriented lamellar mode of EDTA-B organoclay the adsorption priority to iron(III) ions rather than the exfoliated mode in case of DMSO-B. The lamellar modifying scenario in the understudied organoclays besides the predominance adsorbability of Fe³⁺ ions onto EDTA-B are illustrated in Fig. 8a.

In the case of EDTA-B organoclay, EDTA molecules are intercalated within the clay layers by stabilizing their carboxylic groups (COOH) to the oxygen bridges, mainly Si–O–Si siloxane bridges, of clay via hydrogen bonding, *cf.* Fig. 8a. This EDTA-clay linkage widens the clay interlamellar spacings giving rise to an ordered lamellar arrangement, which magnificently feasible Fe³⁺ adsorption onto clay sheets by following several tactics. Firstly, the homogeneity of clay lamellar structure provokes the generation of plenteous sites of adequate adsorption energy like Si–O–Si and Al–O–Si oxygen bridges. Such surface uniformity in the EDTA-B sample was kind consistent with the deduced clay lamellar stacking ordered mode from AFM and TEM results. Secondly,

the ordered clay lamellar stacking mats stimulates the EDTA molecules to charge the clay structure by additionally efficient adsorption sites (deprotonated carboxylic species, COO⁻) (Fig. 8a). These sites are acknowledged to be electrostatically bound to Fe³⁺ ions with adsorption rates.

To underscore the valuable contribution of COO⁻ species in Fe³⁺ adsorption, the experimental q_e value deduced from the adsorption isotherm of the EDTA-B sample in Fig. 7a is compared with the calculated Fe³⁺ adsorbed quantity (q_e , mg/g) over COO⁻ species of EDTA-B, which is theoretically calculated from the given EDTA wt.% fractions to clay lamellar structure (8 wt.%), the molar masses of iron and edetate ions, and the assumed occupancy of each EDTA molecule by two adsorbed Fe³⁺ ions, *cf.* Fig. 8a. Such comparison shows reasonable congruence of the experimental q_e value (=37 mg/g) to the theoretical ones (~32 mg/g). The sensational increase in the measured amount of adsorbed iron ions at the expense of the theoretical value may possibly attribute to the adsorption affinity of other sites such as Si–O–Si and Al–O–Si oxygen bridges.

Lastly, the widening in the interlayered spacings relatively ameliorates the swelling nature of clay facilitating adsorption of the flux of Fe^{3+} ions onto the hard-to-target adsorption sites within the clay lamellar structure. For the sake of convenience, the effect of different used organo-modifiers on the swelling property of clay is examined. The SI of EDTA-B organoclay (~39 mL, being close to the obtained SI by Tunisian clay [61]) is approximately three-fold increasing that registered by the DMSO-B sample (~16 mL) (Fig. 8a), inferring the grand accessibility of clay lamellae to expand and expose the more hidden clay adsorption sites to Fe^{3+} ions in aqueous solution. Such an increase in the SI of EDTA-B is also coincident with the increased BET surface area when compared to DMSO-B.

On the other hand, clay modification by DMSO hypothetically results in roughness and exfoliation of the clay structure (Fig. 8a) giving lamellae of high ζ -potentials, as being evidenced from XRD, surface charge, TEM, and AFM studies. Disagreement in the literature showing that exfoliation of clay platelets not only improves their electrical and morphological properties but also extends their efficient use in several processes of industrial, environmental, and biological interests [28,32,62], clay modification by DMSO molecules weakens the uptake affinity (adsorption rate and capacity) of clay sites toward iron ions. This weird phenomenon is most probably attributed to the oxidizing nature of DMSO molecules that encourages their interaction with the oxygen bridges in clay structure, generating plenty of silanols and/or aluminol hydroxyls (Fig. 8a), as being distinguished from FTIR and ζ -potential studies. The formed hydroxyls are not only concerned to link with Fe^{3+} ions from the produced water via conducting ion-dipole interactions, but also engaged with DMSO molecules by being hydrogen-bonded to the sulfinyl oxygen atom ($-\text{S}=\text{O}$), cf. Fig. 8a.

Doubtlessly, the consensus in this study is in the exact recognition to what extent altering in clay lamellar order can be not only appreciated for Fe^{3+} removal, but also serviceable for removal of most of the tremendous scale-forming cations (like Mg^{2+} , Ca^{2+} , and Sr^{2+}) from produced water. Hence, the applicability of the as-prepared organoclays in removing a wide range of scaling cations from produced water is an indispensable demand by far.

3.3. Uptake studies for removal of Mg^{2+} , Ca^{2+} , and Sr^{2+} scaling cations from artificially produced water using various understudied organoclays

For complete clarification of the potential role of organo-modifier in controlling the adsorption efficiency of bentonite clay, the removal performance of DMSO-B and EDTA-B organoclay for Mg^{2+} , Ca^{2+} , and Sr^{2+} scaling ions are studied, as shown in Fig. 8b. It is clearly discernable that EDTA-B almost exhibits much higher removal performances for the tested scaling ions than those of DMSO-B. Such a phenomenon runs in harmony with the advanced adsorption mechanistic action of Fe^{3+} ions onto EDTA-B sample, cf. Fig. 8a. As regards, the adsorption kinetics of EDTA-B organoclay for Mg^{2+} , Ca^{2+} , and Sr^{2+} scaling ions are studied, and their kinetic curves as well as kinetic parameters, including pseudo-second-order, Fickian diffusion,

and Elovich models, are represented in Table 5, Fig. 8c and Fig. S3. It is obvious that the adsorption affinity of EDTA-B organoclay toward Mg^{2+} , Ca^{2+} , and Sr^{2+} ions increases rapidly within the first 25 min with the removal of more than 85% of the corresponding equilibrium adsorption capacities (Fig. 8c). All the obtained adsorption kinetic parameters give the coefficient of determination (r^2) values near to unity, indicating the neat concurrence of the adsorption progressions of Mg^{2+} , Ca^{2+} , and Sr^{2+} onto EDTA-B to that correspondingly proceeded during Fe^{3+} adsorption. Comparing to the kinetics of Fe^{3+} adsorption onto EDTA-B, the pseudo-second-order rate constants and Elovich coefficients for EDTA-B increase, according to the scaling ions used, in the order: $\text{Fe}^{3+} < \text{Mg}^{2+} < \text{Ca}^{2+} < \text{Sr}^{2+}$ (viz. from 0.009 $\text{g mg}^{-1} \text{min}^{-1}$ for Fe^{3+} to 0.043 $\text{g mg}^{-1} \text{min}^{-1}$ for Sr^{2+} and from 6.26 $\text{mg g}^{-1} \text{min}^{-1}$ for Fe^{3+} to 13.04 $\text{g mg}^{-1} \text{min}^{-1}$ for Sr^{2+} , respectively), Tables 4 and 5. Meanwhile, in a reverse trend, the intraparticle diffusion rate constants for EDTA-B decrease, according to the nature of adsorbate used, in the order: $\text{Fe}^{3+} > \text{Mg}^{2+} > \text{Ca}^{2+} > \text{Sr}^{2+}$ (viz. from 7.25 $\text{mg g}^{-1} \text{min}^{-0.5}$ for Fe^{3+} to 6.57 $\text{mg g}^{-1} \text{min}^{-0.5}$ for Mg^{2+} to 6.03 $\text{mg g}^{-1} \text{min}^{-0.5}$ for Ca^{2+} to 5.56 $\text{mg g}^{-1} \text{min}^{-0.5}$ for Sr^{2+}), Tables 4 and 5. Such contradiction in the order of adsorption kinetic parameters is most probably attributed to the increasing trend in the size of the scaling ions from Fe^{3+} to Mg^{2+} to Ca^{2+} to Sr^{2+} , as their adsorption rates and electrostatic-interacting tendency to carboxylate anions of EDTA ($-\text{COO}^-$) seem to be accelerated by increasing the size of the scaling ions but with the presence of some complications in the diffusion of the large-sized scaling ions within the pore structure of the organoclay [63,64].

Although the adsorption capacity of EDTA-B toward Fe^{3+} ions fails to compensate for a few of adsorbent literature like chemically-modified chitosan/resin composites [59,60], the efficient use of this sample as a generic adsorbent for scale-forming cations most probably seeds it as an invincible and indispensable purification agent for oilfield produced wastewater.

3.4. Pilot plant assessment of the performance of EDTA-B organoclay throughout the process of treating Abu-Rudeis oilfield produced water

On the behalf of the unique lamellar structure of the EDTA-B sample (as lamellae are tuned adopting a long-range ordered and well-dimensioned stacking manner), and its recorded elevated performances (%) for removal of various scale-forming cations from artificially produced water, EDTA-B deserves to be widely examined in the oilfield applications as a promising remover to the scaling cations from OPW, an anti-corrosion agent for steel pipelines and a bio-killer for undesirable microorganisms (such as SRB) in OPW.

3.4.1. Removal performance for various scale-forming cations

Turning to the accepted procedure for setting-up a fundamental pilot experiment in section 2.6., EDTA-B organoclay is examined for the removal of most common scale-forming cations like Fe^{3+} , Mg^{2+} , Ca^{2+} , and Sr^{2+} from Abu-Rudeis oilfield produced water adopting six consecutive purification runs. Each run is conducted for one month

Table 5

Pseudo-second-order kinetics, and Fickian diffusion and Elovich model parameters for removal of Mg^{2+} , Ca^{2+} and Sr^{2+} ions from artificial produced water using EDTA-B organoclay (pH: 2.8; clay content: 2 g/L; initial concentrations: Mg^{2+} 1,564 mg/L, Ca^{2+} 2,713 mg/L, Sr^{2+} 104 mg/L; temperature: 298 K)

Scale-forming cations	Pseudo-second-order model		Fickian diffusion model		Elovich model	
	$k_2 \times 10^2$ (g mg ⁻¹ min ⁻¹)	r^2	k_i (mg g ⁻¹ min ^{-0.5})	r^2	α (mg g ⁻¹ min ⁻¹)	r^2
Mg^{2+}	3.83	0.98	6.57	0.97	6.92	0.99
Ca^{2+}	4.01	0.99	6.03	0.97	11.82	0.98
Sr^{2+}	4.30	0.99	5.56	0.98	13.04	0.99

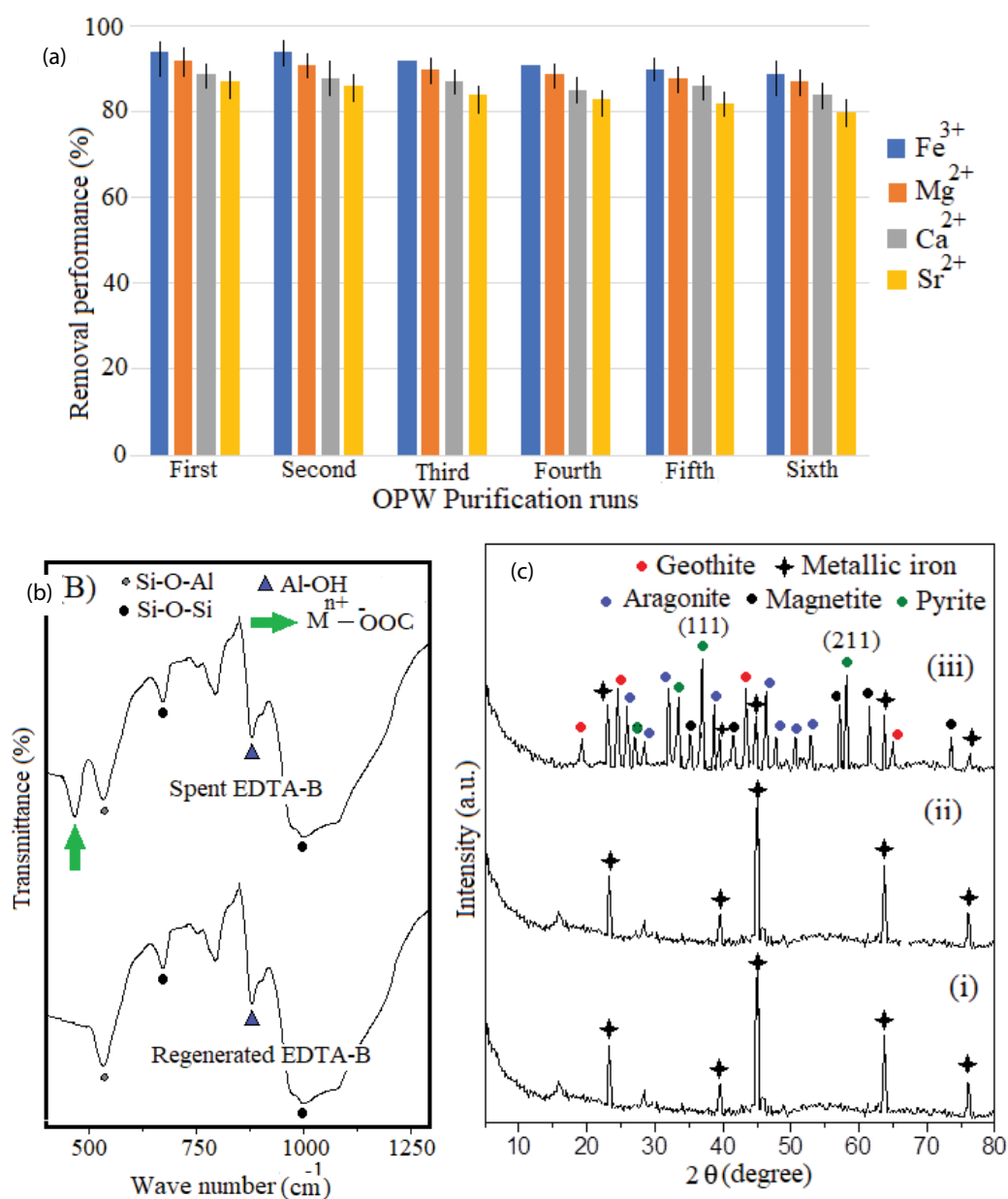


Fig. 9. (a) The % removal performances of the scale-forming cations from OPW by EDTA-B organoclay as a function of the purification runs (pH: 2.8; clay content: 2 g/L; initial concentrations: Fe^{2+} 50 mg/L, Mg^{2+} 1,564 mg/L, Ca^{2+} 2,713 mg/L, Sr^{2+} 104 mg/L; temperature: 298 K; time: 4 h), (b) FTIR spectra of the regenerated and spent EDTA-B organoclay in the sixth purification run, and (c) XRD patterns of: (i) mother X-70 steel coupon, (ii) tested coupon by fundamental experiment and (iii) tested coupon by blank experiment.

after which the spent EDTA-B adsorbent is regenerated and reused in the next purification run. As shown by Fig. 9a, EDTA-B organoclay significantly overcomes blockage of active adsorbing centers during multi-repetitive regeneration/reuse processes, almost keeping the adsorption centers stable and efficient for removal of all the tested scaling ions with achieving performances $\geq 85\%$. Such a phenomenon may strongly infer the beneficial role of the ordered lamellar structure of clay to embrace EDTA molecules and provide them with a balanced interacting mode with the scale-forming cations, as the strength of this interaction is developed during the adsorption process and demolished during the regeneration step. To address this suggestion, the FTIR spectra of the regenerated and the spent EDTA-B sample in the sixth purification run are studied and presented in Fig. 9b. It is clearly observed that the spent EDTA-B is distinguished from the regenerated EDTA-B sample by possessing an additional sharp band at 461 cm^{-1} , which is probably corresponded to the $\text{M}^{\text{n+}}-\text{O}$ vibration modes between carboxylate anions ($-\text{COO}^-$) of EDTA and the various adsorbed scaling cations [65,66]. The position of this band seems to be relevant to that found in metal-EDTA complex salts and metal-EDTA complexes intercalated clays reported in previous works [54,55]. Interestingly, the position and the intensity of the characteristic bands of silanols and aluminols (Fig. 9b) in the FTIR spectrum of spent EDTA-B samples are kept unchanged, indicating the stability of the EDTA-B clay lamellar structure even after six purification runs. Given the observed unceasingly elevations for the removal performances (%) of Fe^{3+} , Mg^{2+} , Ca^{2+} , and Sr^{2+} ions in Fig. 9a, EDTA-B organoclay is strongly qualified to be a superb adsorbent to any scale-forming cations from Oilfield

PW with eminent removal performances over any existing adsorbent in literature, as most of the currently used adsorbents suffer a declined removal performance by reusing [13,17,27,56,60,67].

A comparison of the removal performances (%) of various hazardous ions by different depolluting materials using diverse depollution techniques is listed in Table 6. It is worth mentioning that using the EDTA-B clay sample as an adsorbent opening the door to the adsorption process to retrieve its status as one of the extraordinary depollution techniques for the removal of metal cations. Removal of metal ions, particularly, Fe^{3+} and Sr^{2+} , using EDTA-B clay sample displays much higher efficiencies than those obtained by other exciting depolluting materials in literature by applying either nanofiltration [18,19] or electro dialysis [23] or electrocoagulation/flotation [22] or adsorption [27,59,60] technologies. Moreover, the removal efficiency of EDTA-B for Mg^{2+} and Ca^{2+} ions are highly improved compared to those recorded by other advanced depollution technologies, for example, the electrosorption process [68,69] and precipitation process [70,71], cf. Table 6.

3.4.2. Corrosion protection behavior of steel pipelines

For assessment of the corrosion feature of steel pipelines in Abu-Rudeis oilfield and the protecting behavior of the EDTA-B sample for steel corrosion, immaculate X-70 steel coupons are undertested throughout a blank and fundamental experiments, as being demonstrated in section 2.6. At the end of the six-month exposure period to OPW, the tested coupons are collected from both experiments and the detailed structure of corrosion products, as well as the

Table 6

Comparison of removal performances (%) of various depolluting materials for several pollutant metal ions following diverse depollution processes

Depollution processes	Depolluting materials	Pollutant ions (% removal)	References
Nanofiltration process	Polyethersulphone membrane modified with curcumin boehmite NPs	Fe^{3+} (73); Cu^{2+} (68); Mn^{2+} (66); Pb^{2+} (67); Ni^{2+} (69); Zn^{2+} (70)	[18]
	Polyvinylidene fluoride/ SnO_2 ion exchange membrane	Cd^{2+} (70); Cu^{2+} (92); Ni^{2+} (61); Pb^{2+} (89); Zn^{2+} (77)	[19]
Electrodialysis process	(Chitosan-co-activated carbon) onto (polyvinyl chloride-co-resin) layer by layer ion exchange membrane	Cu^{2+} (72); Ni^{2+} (67); Pb^{2+} (49)	[23]
Electrocoagulation/flotation process	Steel electrodes	Se^{4+} (55); Sr^{2+} (63); Cr^{6+} (74)	[22]
	Titanium electrodes	As^{3+} (75); Cd^{2+} (81); Cu^{2+} (69); Zn^{2+} (76)	[22]
Electrosorption process	Calcium selective nanocomposite electrode	Ca^{2+} (80)	[68]
	N-substituted pyridines based SiO_2 core-shell nanocomposites	Ca^{2+} (32); Ni^{2+} (73)	[69]
Precipitation process	Sodium phosphate precipitant	Mg^{2+} (82)	[70]
	Ammonium phosphate precipitant	Mg^{2+} (98)	[70,71]
Adsorption process	Natural zeolite	Fe^{3+} (62)	[59]
	Organo-modified chitosan/resin composites	Fe^{3+} (100)	[60]
	Activated carbon	Fe^{3+} (56)	[59]
	Poly(styrene butadiene-co-acrylonitrile) NPs	Ba^{2+} (95); Sr^{2+} (87)	[27]
	EDTA-B intercalated organoclay	Fe^{3+} (97); Mg^{2+} (95); Ca^{2+} (90); Sr^{2+} (87)	This study

scale morphologies, are planned to be gained from XRD and SEM analyses. The annotated diffractograms displayed in Fig. 9c show that the peaks characteristic to the α -Fe substrate (ICDD-PDF 04-007-9753, [16]) of the mother X-70 steel coupon are intact by subjecting this coupon to OPW treated with EDTA-B in the fundamental experiment. This finding indicates the superior anti-corrosion behavior of EDTA-B organoclay reflecting most probably the great tendency of EDTA molecules to interact with the scale-forming cations from OPW, thus omits the main reason for scale deposition. Such interpretation is in line with the previously explained adsorption studies. In contrast, the tested coupon from the blank experiment presents additional peaks (Fig. 9c), which are assigned seemingly to mixed crystalline scale deposits, including pyrite (JCPDS No. 06-0710), aragonite (JCPDS No. 01-0628), goethite (JCPDS No. 17-0536) and magnetite (JCPDS No. 87-2334) [72–75]. The pyrite is relatively the predominant crystalline scale deposit of distinctly higher peak intensities than any other formed scale, exhibiting an octahedron morphology with intense diffractions by well-resolved (111) and (211) lattice

fringes at 2θ equate 35° (of d -spacing = 3.16 \AA) and 58.5° (of d -spacing = 2.24 \AA), respectively [72], Fig. 9c.

SEM imaging at various magnifications has been used to investigate the morphological changes in the mother X-70 steel coupon after the suspension corrosion tests (Fig. 10). Mother X-70 steel coupon shows smooth and platy Fe surfaces with virtually no morphological changes after the fundamental corrosion experiment, even little darkening is observed by mother coupon when subjected to a flow of OPW in presence of EDTA-B organoclay, *cf.* Figs. 10a and b and their inset images. This finding is highly in compliance with the obtained XRD results. On the other hand, the tested coupon drawn from the blank corrosion experiment displays a considerable amount of scaling friable deposits (Fig. 10c), which are loosely located onto the Fe surface and have a light brown color (inset of Fig. 10c). The pyrite scale majorly appears as blocks of shiny aggregated crystals (as represented by the yellow arrows in Fig. 10c) showing roughly octahedral shape with clear edges (as represented from inset image 1, which magnifies the contents in the green dashed circle in Fig. 10c). The aragonite (calcite scale)

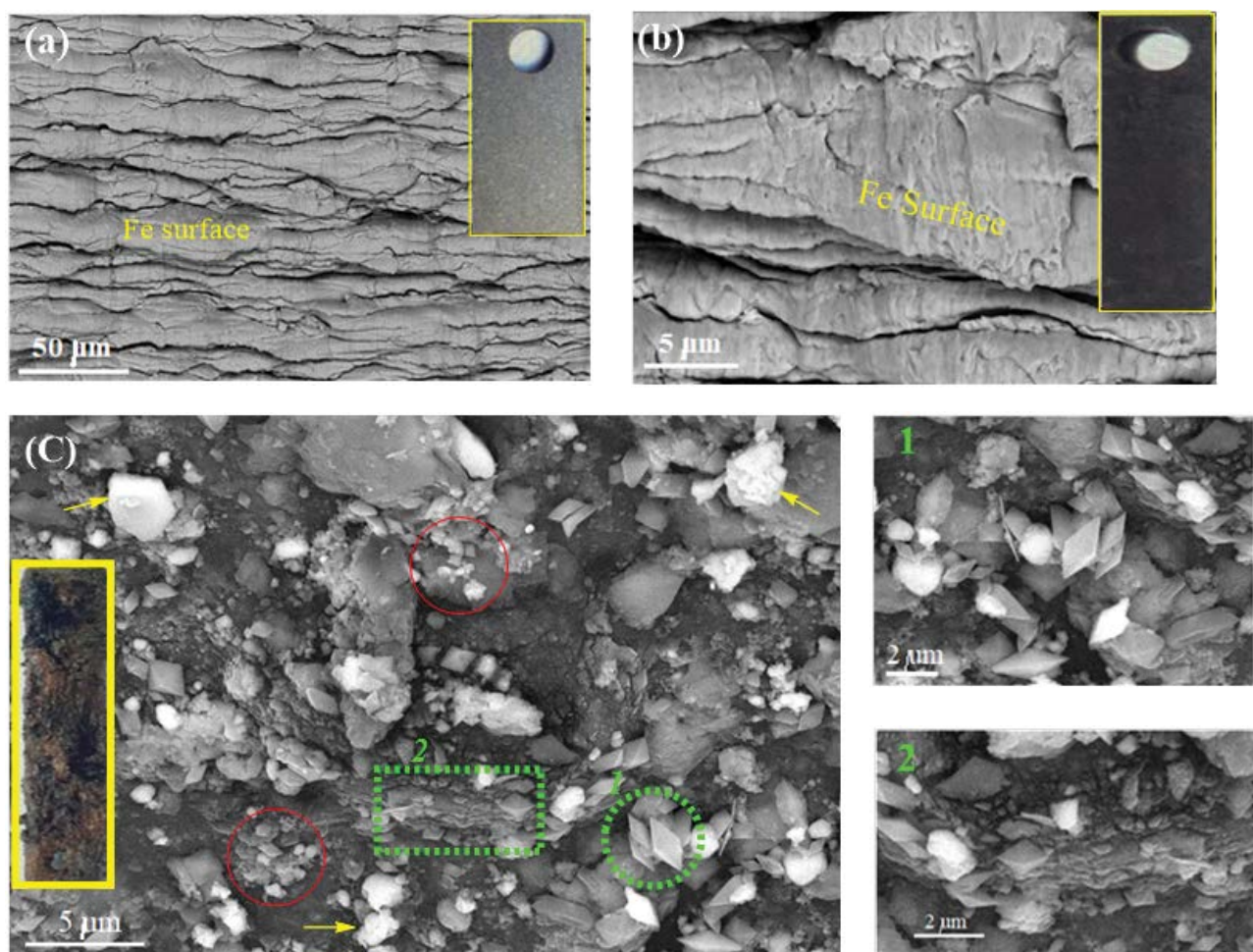


Fig. 10. SEM micrographs of (a) mother X-70 steel coupon, (b) tested coupon by fundamental experiment, and (c) tested coupon by blank experiment. The inset camera digital images reflect the changes in the facial surface of coupons under study, and the inset images (1 and 2) in micrograph C show magnified views for corrosion products.

possesses irregular shaped micro-sized granules that seem to adhere on the pyrite aggregation blocks, as clarified by red circles in Fig. 10c. The iron oxide scale seems to form compact rust layers with jagged edges at which pyrite particles are attached, as demonstrated by a green dashed rectangle in Fig. 10c and its magnified image 2. As a result, deposition of all these scales on the tested coupon perhaps limits the presence of metallic Fe surfaces, which seems to be entirely corroded.

For more confirmation, LSI measurement is carried out to estimate the corrosivity of the treated OPW by EDTA-B suspension [14]. The LSI values of the obtained OPW from blank and fundamental experiments record -4.5 and -0.2 , respectively, indicating the great capability of EDTA-B to discharge the corrosiveness of the oilfield produced water and antagonize its scale-forming tendency. Furthermore, the anti-corrosive nature of EDTA-B is assessed by detecting the MLDR value, which reveals the improved level of EDTA-B clay suspension in OPW onto the steel corrosive resistance to achieve $\sim 94\%$. However, still many tests need to be performed to interpret the anticorrosive behavior of EDTA-B organoclay for steel and metal containers in future publications, for example, electrochemical, corrosion wear-resistant, discoloration, and gloss measurements.

3.4.3. Biocide performance against SRB

Turning to the qualitative description of scaling from XRD and SEM studies, having established pyrite as the main corrosion product strongly anticipates the existence of anaerobic SRB microorganism in the produced water from Abu-Rudeis oilfield. In this respect, the biocidal activities of DMSO-B and EDTA-B organoclays against SRB are studied and compared to that of the R-B clay sample following the procedure in section 2.7. As can be seen from Figs. 11a and b, the production of planktonic and sessile SRB cells are profoundly deteriorated by using the understudied clay samples in the order: EDTA-B > DMSO-B > R-B. The EDTA-B organoclay displays a greater inhibitory effect

toward the production of SRB yielding biocidal efficacy of 97% and 91% against planktonic and sessile cells, respectively. These results resemble the killing efficiency of SRB by bacterium *Bacillus licheniformis*, sanitizers, and recombinant *Pseudomonas stutzeri* Rhl [52,76,77]. The biocide performance of EDTA-B can be attributable to the anti-inflammatory characteristics of bentonite clay [78], and the potential antimicrobial nature of EDTA molecule, which acts as an efficient chelator for removal of Mg^{2+} and Ca^{2+} ions from the outer cell wall of bacteria [79].

4. Concluding remarks

In this study, the authors focused on the organo-modification of Egyptian bentonite clay by common molecules like EDTA and DMSO to proceed with intercalated and exfoliated systems, respectively. The formed organoclays were characterized by XRD, FTIR, DLS, N_2 -physisorption, AFM, and TEM techniques.

In summary, building up a long-range ordered and intercalated stacks of laminated clays with well-dimensioned hexagon-shaped architecture was much more appreciated in the petroleum industry than constructing a clay exfoliating system. A concept that contradicts nowadays scientific directions in finding out exfoliation as a second field to widen the clays applications for environmental and industrial purposes. Such unique clay lamellar orientation was facilitated by intercalating and stabilizing EDTA molecules onto Si–O–Si bridges of bentonite clay via hydrogen bonding. The formed organoclay exhibited developed surface area with highly uniform micro-sized pore structure, and even negatively charged lamellae ($\zeta_{av} = -26.5$ mV) of elevated swelling nature ($SI = 39$ mL). In contrast, DMSO molecules markedly degenerated the oxygen bridges of the clay structure, creating delicate roughened lamellar exfoliated particles of uneven highly negative charges and poor surface character. Both clay systems were examined in the removal of various scaling cations (Fe^{3+} , Mg^{2+} , Ca^{2+} , and Sr^{2+}) from artificially produced water. The intercalated clay

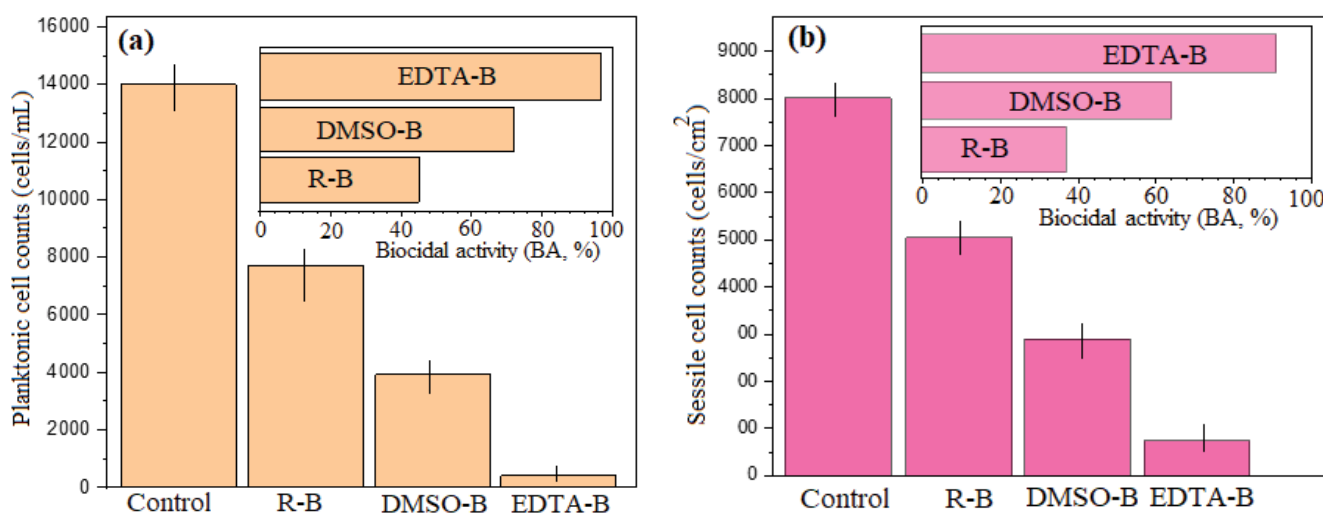


Fig. 11. Counts of SRB (a) planktonic and (b) sessile cells after 20 d in the control experiment and the inoculated Abu-Rudeis oilfield produced water. Insets: biocidal activities of the understudied samples against planktonic and sessile SRB cells.

system was a candidate as superb adsorbent that allows the carboxylate anions of EDTA intercalant to electrostatically interact with the scalant ions. Such adsorption progression was set-up over highly energetic homogeneous surfaces following Langmuir and D–R isotherm models of pseudo-second-order kinetics linked with elevated adsorption rates and removal efficiency close to 90%.

On this basis, EDTA-B organoclay was successfully deployed in Abu-Rudeis oilfield as a low-cost adsorbent for the scale-forming cations from OPW, corrosion-protection agent for steel pipelines and biocidal against the presence of various SRB species in OPW. The EDTA-B profoundly removed all the scaling cations with long-term durability in the repeating regeneration/reuse purification runs owing removal performances $\geq 85\%$. Also, EDTA-B exhibited superior anti-corrosion behavior for steel pipelines with almost entire inhibition of scale formation, and near 100% SRB biocide activity. Studying variant intercalated clay systems for industrial and environmental applications promise immense potential in the near future.

Acknowledgments

The authors are thankful to Belayim Petroleum Company (Petrobel, Egypt) and feel deeply indebted to the thorough efforts of the chemical engineers and biologists who generously gave us much help and valuable information concerning the produced water analysis and processing in Abu-Rudeis oilfield.

References

- [1] N.H. Alias, J. Jaafar, S. Samitsu, T. Matsuura, A.F. Ismail, M.H.D. Othman, M.A. Rahman, N.H. Othman, N. Abdullah, S.H. Paiman, N. Yusof, F. Aziz, Photocatalytic nanofiber-coated alumina hollow fiber membranes for highly efficient oilfield produced water treatment, *Chem. Eng. J.*, 360 (2019) 1437–1446.
- [2] Z.Z. Ismail, M.A. Ibrahim, Desalination of oilfield produced water associated with treatment of domestic wastewater and bioelectricity generation in microbial osmotic fuel cell, *J. Membr. Sci.*, 490 (2015) 247–255.
- [3] X. Huang, J. Wang, C.Y. Ma, L.Y. Ma, C. Qiao, Diversity analysis of microbial communities and biodegradation performance of two halotolerant and thermotolerant *Bacillus licheniformis* strains in oilfield-produced wastewater, *Int. Biodeterior. Biodegrad.*, 137 (2019) 30–41.
- [4] R.N. Zhang, Y.N. Liu, M.R. He, Y.L. Su, X.T. Zhao, M. Elimelech, Z.Y. Jiang, Antifouling membranes for sustainable water purification: strategies and mechanisms, *Chem. Soc. Rev.*, 45 (2016) 5888–5924.
- [5] G. Silva, B. Correia, A. Cunha, B. Santos, A. Lima, Water injection for oil recovery by using reservoir simulation via CFD, *Int. J. Multiphys.*, 11 (2017) 83–96.
- [6] J. Li, Y. Wang, S.L. Li, L.P. Fang, G.C. Hou, B.Y. Shi, Water quality deterioration of treated oilfield injection water in the water distribution system of the Jiangnan oilfield, *Water Supply*, 19 (2018) 519–526.
- [7] A. Fakhru'l-Razi, A. Pendashteh, L.C. Abdullah, D.R.A. Biak, S.S. Madaeni, Z.Z. Abidin, Review of technologies for oil and gas produced water treatment, *J. Hazard. Mater.*, 170 (2009) 530–551.
- [8] A. Motta, A. Kiperstok, C. Borges, K. Esquerre, Oil produced water treatment for oil removal by an integration of coalescer bed and microfiltration membrane processes, *J. Membr. Sci.*, 469 (2014) 371–378.
- [9] B. He, L.J. Zhang, Q.H. Zhu, J. Wang, X. Yun, J.S. Luo, Z.K. Chen, Effect of solution treated 316L layer fabricated by laser cladding on wear and corrosive wear resistance, *Opt. Laser Technol.*, 121 (2020) 105788–105796.
- [10] P. Sarin, V.L. Snoeyink, D.A. Lytle, W.M. Kriven, Iron corrosion scales: model for scale growth, iron release, and colored water formation, *J. Environ. Eng.*, 130 (2004) 364–373.
- [11] Z.Q. Wang, Z.Y. Zhou, W.C. Xu, L.H. Yang, B.B. Zhang, Y.T. Li, Study on inner corrosion behavior of high strength product oil pipelines, *Eng. Fail. Anal.*, 115 (2020) 104659–104671.
- [12] P. Zhang, D. Shen, G.D. Ruan, A.T. Kan, M.B. Tomson, Phosphinopolycarboxylic acid modified inhibitor nanomaterial for oilfield scale control: synthesis, characterization and migration, *J. Ind. Eng. Chem.*, 45 (2017) 366–374.
- [13] M. Chen, K. Shafer-Peltier, M. Veisi, S. Randtke, E. Peltier, Complexation and precipitation of scale-forming cations in oilfield produced water with polyelectrolytes, *Sep. Purif. Technol.*, 222 (2019) 1–10.
- [14] S. Acharya, S.K. Sharma, V. Khandegar, Assessment and hydrogeochemical characterization for evaluation of corrosion and scaling potential of groundwater in South West Delhi, India, *Data Brief*, 18 (2018) 928–938.
- [15] P. Zhang, Y. Liu, S.C. Kuok, A.T. Kan, M.B. Tomson, Development of modeling approaches to describe mineral scale deposition kinetics in porous medium and pipe flow system, *J. Petrol. Sci. Eng.*, 178 (2019) 594–601.
- [16] G.R. Joshi, K. Cooper, X.L. Zhong, A.B. Cook, E.A. Ahmad, N.M. Harrison, D.L. Engelberg, R. Lindsay, Temporal evolution of sweet oilfield corrosion scale: phases, morphologies, habits, and protection, *Corros. Sci.*, 142 (2018) 110–118.
- [17] X.-X. Li, J.-F. Liu, F. Yao, W.-L. Wu, S.-Z. Yang, S.-M. Mbadanga, J.-D. Gu, B.-Z. Mu, Dominance of *Desulfotogium* in sulfate-reducing community in high sulfate production-water of high temperature and corrosive petroleum reservoirs, *Int. Biodeterior. Biodegrad.*, 114 (2016) 45–56.
- [18] G. Moradi, S. Zinadini, L. Rajabi, A.A. Derakhshan, Removal of heavy metal ions using a new high performance nanofiltration membrane modified with curcumin boehmite nanoparticles, *Chem. Eng. J.*, 390 (2020) 124546–124560.
- [19] Y. Ibrahim, V. Naddeo, F. Banat, S.W. Hasan, Preparation of novel polyvinylidene fluoride (PVDF)-Tin(IV) oxide (SnO_2) ion exchange mixed matrix membranes for the removal of heavy metals from aqueous solutions, *Sep. Purif. Technol.*, 250 (2020) 117250–117264.
- [20] S.H. Ammar, A.S. Akbar, Oilfield produced water treatment in internal-loop airlift reactor using electrocoagulation/flotation technique, *Chin. J. Chem. Eng.*, 26 (2018) 879–885.
- [21] M. Prica, S. Adamovic, B. Dalmacija, L. Rajic, J. Trickovic, S. Rapajic, M. Becelic-Tomin, The electrocoagulation/flotation study: The removal of heavy metals from the waste fountain solution, *Process Saf. Environ. Prot.*, 94 (2015) 262–273.
- [22] M.M. Emamjomeh, M. Sivakumar, Review of pollutants removed by electrocoagulation and electrocoagulation/flotation processes, *J. Environ. Manage.*, 90 (2009) 1663–1679.
- [23] S.M. Hosseini, H. Alibakhshi, E. Jashni, F. Parvizian, J.N. Shen, M. Taheri, M. Ebrahimi, N. Rafiei, A novel layer-by-layer heterogeneous cation exchange membrane for heavy metal ions removal from water, *J. Hazard. Mater.*, 381 (2020) 120884–120893.
- [24] S.A. Dastgheib, C. Knutson, Y. Yang, H.H. Salih, Treatment of produced water from an oilfield and selected coal mines in the Illinois Basin, *Int. J. Greenhouse Gas Control*, 54 (2016) 513–523.
- [25] M. Lu, X.F. Wei, Treatment of oilfield wastewater containing polymer by the batch activated sludge reactor combined with a zerovalent iron/EDTA/air system, *Bioresour. Technol.*, 102 (2011) 2555–2562.
- [26] J. Wu, R.J. Zeng, F. Zhang, Z.G. Yuan, Application of iron-crosslinked sodium alginate for efficient sulfide control and reduction of oilfield produced water, *Water Res.*, 154 (2019) 12–20.
- [27] S.A. Younis, M.M. Ghobashy, G. Bassioni, A.K. Gupta, Tailored functionalized polymer nanoparticles using gamma radiation for selected adsorption of barium and strontium in oilfield wastewater, *Arabian J. Chem.*, 13 (2020) 3762–3774.

- [28] S.A. Hassan, A.S. Darwish, H.M. Gobara, N.E.A. Abed-Elstatar, S.R. Fouda, Interaction profiles in poly (amidoamine) dendrimer/montmorillonite or rice straw ash hybrids-immobilized magnetite nanoparticles governing their removal efficiencies of various pollutants in wastewater, *J. Mol. Liq.*, 230 (2017) 353–369.
- [29] S.A. Hassan, F.Z. Yehia, H.A. Hassan, S.A. Sadek, A.S. Darwish, Various characteristics and catalytic performance of iron(II) phthalocyanine immobilized onto titania- and vanadia-pillared bentonite clay in *in situ* polymerization of methyl methacrylate: an attempt to synthesize novel polymer/iron phthalocyanine/pillared clay nanocomposites, *J. Mol. Catal. A: Chem.*, 332 (2010) 93–105.
- [30] M.A. Mekewi, A.S. Darwish, M.E. Amin, H.A. Bourazan, Sustainable removal of Cu^{2+} , Ni^{2+} and Zn^{2+} ions from severe contaminated water using kaolin/poly(glycine) composites, characterization and uptake studies, *Desal. Water Treat.*, 51 (2013) 7746–7763.
- [31] M.A. Mekewi, A.S. Darwish, M.S. Amin, Gh. Eshaq, H.A. Bourazan, Copper nanoparticles supported onto montmorillonite clays as efficient catalyst for methylene blue dye degradation, *Egypt. J. Pet.*, 25 (2016) 269–279.
- [32] F.E.A. Bayaomy, A.S. Darwish, Exfoliated Egyptian kaolin immobilized heteropolyoxotungstate nanocomposite as an innovative antischistosomal agent: *In vivo* and *in vitro* bioactive studies, *Mater. Sci. Eng., C*, 59 (2016) 717–730.
- [33] G. Choi, H.Y. Piao, Z.A. Allothman, A. Vinu, C.-O. Yun, J.-H. Choy, Anionic clay as the drug delivery vehicle: tumor targeting function of layered double hydroxide-methotrexate nanohybrid in C33A orthotopic cervical cancer model, *Int. J. Nanomed.*, 11 (2016) 337–348.
- [34] S. Kar, B. Kundu, R.L. Reis, R. Sarkar, P. Nandy, R. Basu, S. Das, Curcumin ameliorates the targeted delivery of methotrexate intercalated montmorillonite clay to cancer cells, *Eur. J. Pharm. Sci.*, 135 (2019) 91–102.
- [35] R. Rojas, M. Rosario Perez, E.M. Erro, P.I. Ortiz, M.A. Ulibarri, C.E. Giacomelli, EDTA modified LDHs as Cu^{2+} scavengers: removal kinetics and sorbent stability, *J. Colloid Interface Sci.*, 331 (2009) 425–431.
- [36] E.H. de Faria, O.J. Lima, K.J. Ciuffi, E.J. Nassar, M.A. Vicente, R. Trujillano, P.S. Calefi, Hybrid materials prepared by inter-layer functionalization of kaolinite with pyridine-carboxylic acids, *J. Colloid Interface Sci.*, 335 (2009) 210–215.
- [37] E. Iglesias, Solvent effects vs. concentration effects in determining rates of base-catalyzed keto-enol tautomerization, *New J. Chem.*, 29 (2005) 625–632.
- [38] R.L. Frost, E. Horváth, É. Makó, J. Kristóf, T. Cseh, The effect of mechanochemical activation upon the intercalation of a high-defect kaolinite with formamide, *J. Colloid Interface Sci.*, 265 (2003) 386–395.
- [39] T.A. Elbokl, C. Detellier, Intercalation of cyclic imides in kaolinite, *J. Colloid Interface Sci.*, 323 (2008) 338–348.
- [40] D. Naghipour, H. Gharibi, K. Taghavi, J. Jaafari, Influence of EDTA and NTA on heavy metal extraction from sandy-loam contaminated soils, *J. Environ. Chem. Eng.*, 4 (2016) 3512–3518.
- [41] M.R. Pérez, I. Pavlovic, C. Barriga, J. Cornejo, M.C. Hermosín, M.A. Ulibarri, Uptake of Cu^{2+} , Cd^{2+} and Pb^{2+} on Zn–Al layered double hydroxide intercalated with EDTA, *Appl. Clay Sci.*, 32 (2006) 245–251.
- [42] H.D. Chapman, Cation Exchange Capacity, C.A. Black (Ed.), *Methods of Soil Analysis, Part 2: Chemical and Microbiological Properties*, American Society of Agronomy, Inc., Soil Science Society of America, Inc., Madison, Wisconsin USA, 1965, pp. 891–901.
- [43] K.S.W. Sing, D.H. Everett, R.A.W. Haul, L. Moscou, R.A. Pierotti, J. Rouquerol, T. Siemieniowska, Reporting physisorption data for gas/solid systems with special reference to the determination of surface area and porosity, *Pure Appl. Chem.*, 57 (1985) 603–619.
- [44] S.A. Siddiqi, F. Manzoor, A. Jamal, M. Tariq, R. Ahmad, M. Kamran, A. Chaudhry, I.U. Rehman, Mesenchymal stem cell (MSC) viability on PVA and PCL polymer coated hydroxyapatite scaffolds derived from cuttlefish, *RSC Adv.*, 6 (2011) 32897–32904.
- [45] S.J. Gregg, K.S.W. Sing, *Adsorption, Surface Area and Porosity*, 2nd ed., Academic Press, London, 1982.
- [46] H.M.F. Freundlich, Over the adsorption in solution, *Z. Phys. Chem.*, 57 (1906) 385–470.
- [47] I. Langmuir, The constitution and fundamental properties of solids and liquids. Part I. solids, *J. Am. Chem. Soc.*, 38 (1916) 2221–2295.
- [48] M.M. Dubinin, L.V. Radushkevich, Equation of the characteristic curve of activated charcoal, *Proc. Acad. Sci. Phys. Chem. USSR*, 55 (1947) 331–333.
- [49] M.I. Temkin, V. Pyzhev, Kinetics of ammonia synthesis on promoted iron catalyst, *Acta USSR*, 12 (1940) 327–356.
- [50] K.R. Hall, L.C. Eagleton, A. Acrivos, T. Vermeulen, Pore- and solid-diffusion kinetics in fixed-bed adsorption under constant-pattern conditions, *Ind. Eng. Chem. Fundam.*, 5 (1966) 212–223.
- [51] M.A. Mekewi, T.M. Madkour, A.S. Darwish, Y.M. Hashish, Does poly(acrylic acid-co-acrylamide) hydrogel be the pluperfect choiceness in treatment of dyeing wastewater? “From simple copolymer to gigantic aqua-waste remover”, *J. Ind. Eng. Chem.*, 30 (2015) 359–371.
- [52] H.W. Liu, T.Y. Gu, G. Zhang, H.F. Liu, Y.F. Cheng, Corrosion of X80 pipeline steel under sulfate-reducing bacterium biofilms in simulated CO_2 -saturated oilfield produced water with carbon source starvation, *Corros. Sci.*, 136 (2018) 47–59.
- [53] J.L. Wang, B.S. Hou, J. Xiang, X.D. Chen, T.Y. Gu, H.F. Liu, The performance and mechanism of bifunctional biocide sodium pyrithione against sulfate-reducing bacteria in X80 carbon steel corrosion, *Corros. Sci.*, 150 (2019) 296–308.
- [54] M. Kagan, G.K. Lockwood, S.H. Garofalini, Reactive simulations of the activation barrier to dissolution of amorphous silica in water, *Phys. Chem. Chem. Phys.*, 16 (2014) 9294–9301.
- [55] Z. Papanayan, S. Markarian, Detection of oxidation of L-cysteine by dimethyl sulfoxide in aqueous solutions by IR spectroscopy, *J. Appl. Spectrosc.*, 80 (2013) 775–778.
- [56] X.K. Leng, Y.J. Zhong, D.H. Xu, X.L. Wang, L. Yang, Mechanism and kinetics study on removal of Iron from phosphoric acid by cation exchange resin, *Chin. J. Chem. Eng.*, 27 (2019) 1050–1057.
- [57] K.G. Bhattacharyya, S.S. Gupta, Kaolinite and montmorillonite as adsorbents for Fe(III), Co(II) and Ni(II) in aqueous medium, *Appl. Clay Sci.*, 41 (2008) 1–9.
- [58] E.M.I. Elsehly, N.G. Chechenin, A.V. Makunin, E.A. Vorobyeva, H.A. Motaweh, Oxidized carbon nanotubes filters for iron removal from aqueous solutions, *Int. J. New Technol. Sci. Eng.*, 2 (2015) 14–18.
- [59] M.M.H. Khalil, K.Z. Al-Wakeel, S.S. Abd El Rehim, H. Abd El Monem, Efficient removal of ferric ions from aqueous medium by amine modified chitosan resins, *J. Environ. Chem. Eng.*, 1 (2013) 566–573.
- [60] M.M.H. Khalil, K.Z. Al-Wakeel, S.S. Abd El Rehim, H. Abd El Monem, Adsorption of Fe(III) from aqueous medium onto glycine-modified chitosan resin: equilibrium and kinetic studies, *J. Dispersion Sci. Technol.*, 35 (2014) 1691–1698.
- [61] S. Boussen, D. Sghaier, F. Chaabani, B. Jamoussi, S.B. Messaoud, A. Bennour, The rheological, mineralogical and chemical characteristic of the original and the Na_2CO_3 -activated Tunisian swelling clay (Aleg Formation) and their utilization as drilling mud, *Appl. Clay Sci.*, 118 (2015) 344–353.
- [62] S.A. Abdel-Latef, A.S. Darwish, S.A. Rizk, S.K. Atya, M.H.E. Helal, Morphology control synthesis of iron-rich Sinai clay by novel O, N, S-heterocyclic moieties: magnetic organoclays for various strategic uses in lubricating oilfield industry, *J. Mol. Liq.*, 288 (2019) 111006–111021.
- [63] S. Sircar, Influence of adsorbate size and adsorbent heterogeneity of IAST, *AICHE J.*, 41 (1995) 1135–1145.
- [64] N.N. Greenwood, A. Earnshaw, *Chemistry of the Elements*, 2nd ed., Elsevier Science Publication Company, New York, 1997.

- [65] D.T. Sawyer, P.J. Paulsen, Properties and infrared spectra of ethylenediaminetetraacetic acid complexes. II. Chelates of divalent ions, *J. Am. Chem. Soc.*, 81 (1959) 816–820.
- [66] R. Rojas, M.A. Ulibarri, C. Barriga, V. Rives, Intercalation of metal-EDTA complexes in Ni–Zn layered hydroxysalts and study of their thermal stability, *Microporous Mesoporous Mater.*, 112 (2008) 262–272.
- [67] R.I. Jeldres, M.P. Arancibia-Bravo, A. Reyes, C.E. Aguirre, L. Cortes, L.A. Cisternas, The impact of seawater with calcium and magnesium removal for the flotation of copper-molybdenum sulphide ores, *Miner. Eng.*, 109 (2017) 10–13.
- [68] J. Kim, A. Jain, K.C. Zuo, R. Verduzco, S. Walker, M. Elimelech, Z.H. Zhang, X.H. Zhang, Q.L. Li, Removal of calcium ions from water by selective electrosorption using target-ion specific nanocomposite electrode, *Water Res.*, 160 (2019) 445–453.
- [69] T. Geng, D. Zhao, J. Xu, M. Ren, F.H. Cao, Removal of nickel and calcium from crude oil using core-shell materials grafted with N-substituted pyridines, *J. Petrol. Sci. Eng.*, 195 (2020) 107502–107510.
- [70] L.H. He, W.H. Xu, Y.F. Song, X.H. Liu, Z.W. Zhao, Selective removal of magnesium from a lithium-concentrated anolyte by magnesium ammonium phosphate precipitation, *Sep. Purif. Technol.*, 187 (2017) 214–220.
- [71] C. Xiao, L.S. Xiao, C.J. Gao, L. Zeng, Thermodynamic study on removal of magnesium from lithium chloride solutions using phosphate precipitation method, *Sep. Purif. Technol.*, 156 (2015) 582–587.
- [72] C. Arrouvel, J.-G. Eon, Understanding the surfaces and crystal growth of pyrite FeS_2 , *Mater. Res.*, 22 (2019) 1140–1148.
- [73] A.S. Darwish, F.E.A. Bayaomy, H.M. Ismail, Photoactivated water-disinfecting, and biological properties of Ag NPs@Sm-doped ZnO nanorods/cuttlefish bone composite: *in-vitro* bactericidal, cercaricidal and schistosomicidal studies, *Mater. Sci. Eng., C*, 93 (2018) 996–1011.
- [74] G. Hu, Study of inhibition performance of a vapor phase inhibitor on rusty iron coins, *Am. J. Appl. Chem.*, 4 (2016) 207–211.
- [75] D.-W. Jung, S.-W. Han, B.-S. Kong, E.-S. Oh, Crystal modification of iron oxide scale by potassium addition and its application to lithium-ion battery anodes, *J. Power Sources*, 242 (2013) 357–364.
- [76] F. Zhao, J.-D. Zhou, F. Ma, R.-J. Shi, S.-Q. Han, J. Zhang, Y. Zhang, Simultaneous inhibition of sulfate-reducing bacteria, removal of H_2S and production of rhamnolipid by recombinant *Pseudomonas stutzeri* RhI: applications for microbial enhanced oil recovery, *Bioresour. Technol.*, 207 (2016) 24–30.
- [77] P. Chavant, B. Gaillard-Martinie, M. Hébraud, Antimicrobial effects of sanitizers against planktonic and sessile *Listeria monocytogenes* cells according to the growth phase, *FEMS Microbiol. Lett.*, 236 (2004) 241–248.
- [78] S.H. Emami-Razavi, N. Esmaeili, S.K. Forouzannia, S. Amanpour, S. Rabbani, A.M. Alizadeh, M.A. Mohagheghi, Effect of bentonite on skin wound healing: experimental study in the rat model, *Acta Med. Iran.*, 44 (2006) 235–240.
- [79] S. Finnegan, S.L. Percival, EDTA: an antimicrobial and antibiofilm agent for use in wound care, *Adv. Wound Care*, 4 (2015) 415–421.

Supplementary information

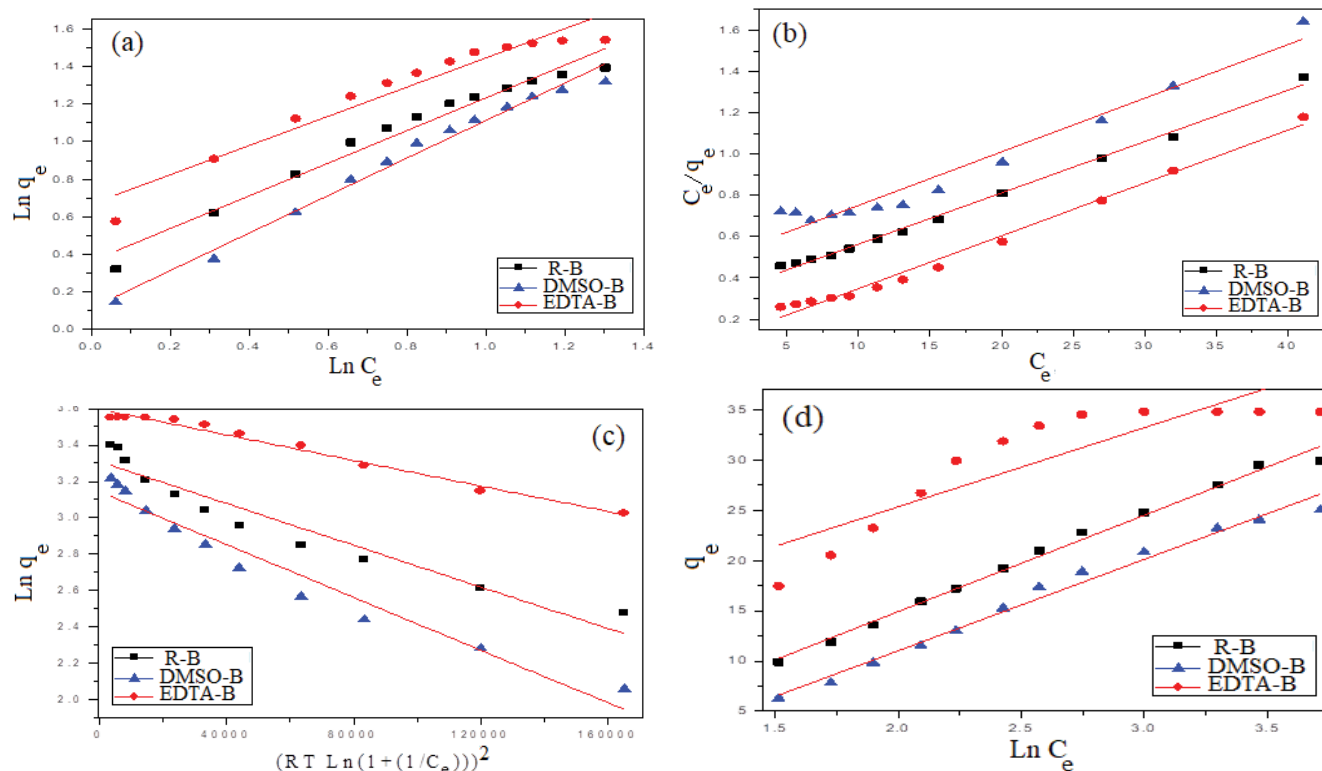


Fig. S1: Freundlich (a), Langmuir (b), Dubinin–Radushkevich (c) and Temkin (d) adsorption isotherm models for adsorption of Fe^{3+} from artificially produced water by various understudied clay samples (pH: R-B 2.0; DMSO-B 3.2; EDTA 2.8; clay content: 2 g/L; initial iron ion concentrations: 10, 20, 40, 50, 70, 90, 120 mg/L; temperature: 298 K; contact equilibrium time: 4 h).

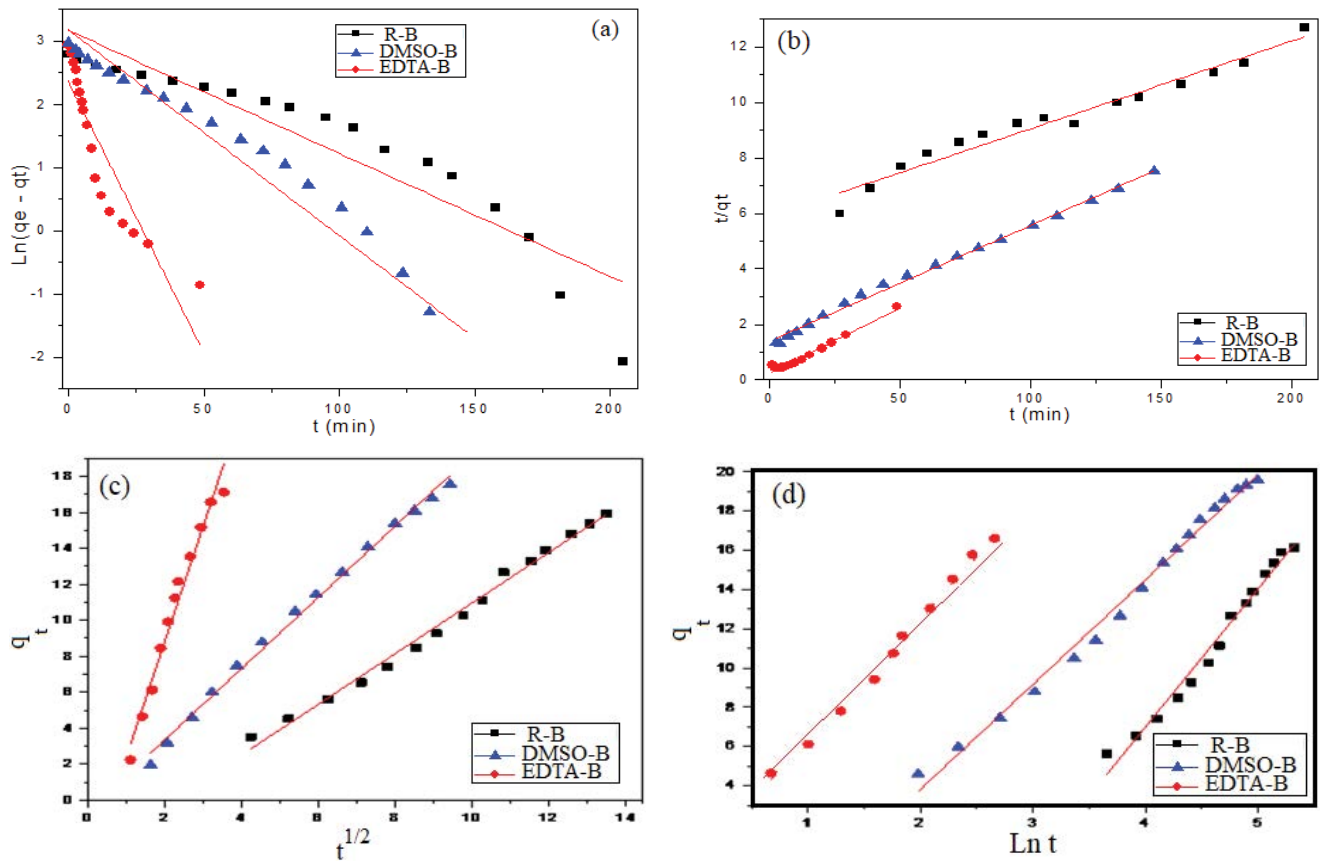


Fig. S2: Pseudo-first-order (a), pseudo-second-order (b), Fickian diffusion (c), as well as Elovich (d) kinetic plots of Fe^{3+} adsorption from artificially produced water using various understudied clays (pH: R-B 2.0; DMSO-B: 3.2; EDTA: 2.8; clay content: 2 g/L; initial iron ion concentrations: 50 mg/L; temperature: 298 K).

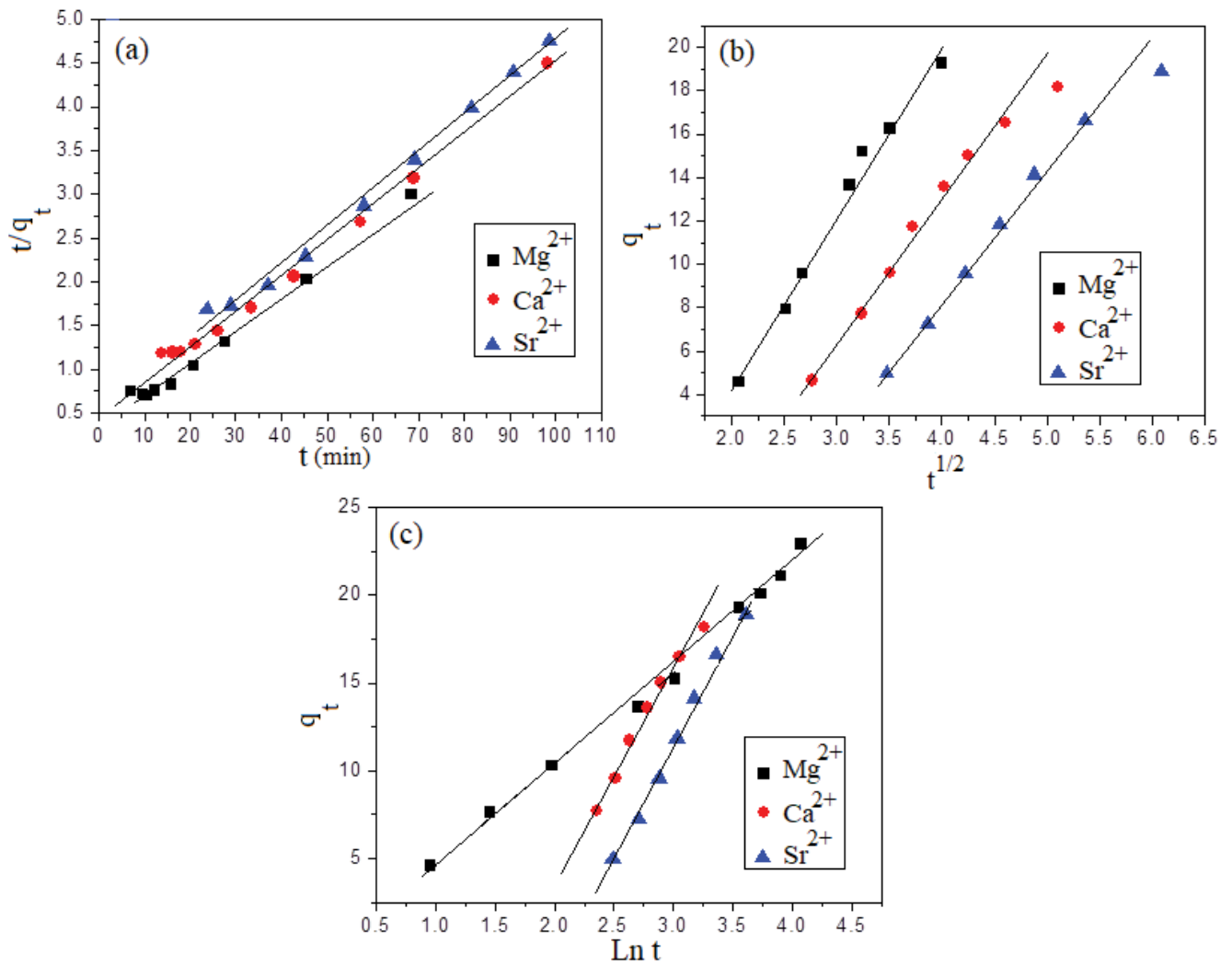


Fig. S3: Pseudo-second-order (a), Fickian diffusion (b), as well as Elovich (c) kinetic plots of adsorption of Mg^{2+} , Ca^{2+} and Sr^{2+} scaling ions from artificially produced water using EDTA-B organoclay (pH: 2.8; clay content: 2 g/L; initial concentrations: Mg^{2+} 1,564 mg/L, Ca^{2+} 2,713 mg/L, Sr^{2+} 104 mg/L; temperature: 298 K).